Active subaquatic fault segments in Lake Iznik along the middle strand of the North Anatolian Fault, NW Turkey

R. Gastineau[1,2], J. de Sigoyer[1], P. Sabatier[2], S.C. Fabbri[3], F.S. Anselmetti[3], AL. Develle[2], M. Şahin[4], S. Gündüz[4], F. Niessen[5] and A. C. Gebhardt[5]

1 Univ. Grenoble Alpes, Univ. Savoie Mont Blanc, CNRS, IRD, IFSTTAR, ISTerre, 38000 Grenoble, France

2 EDYTEM, Université Savoie Mont-Blanc, Université Grenoble Alpes, CNRS, Le Bourget du Lac, France

3 Institute of Geological Sciences and Oeschger Centre for Climate Change Research, University of Bern, Baltzerstrasse 1+3, 3012 Bern, Switzerland

4 Bursa Uludağ Üniversitesi, Fen-Edebiyat Fakültesi, Arkeologi Bölümü, Görükle, Bursa, Turkey.

5 Alfred Wegener Institute (AWI) Helmholtz Centre for Polar and Marine Research, D-27568, Bremerhaven, Germany

Corresponding author: Renaldo Gastineau (renaldo.gastineau@univ-grenoble-alpes.fr)

Key points:

1. Previously unknown faults that belong to the North Anatolian Fault system have been discovered in Lake Iznik through geophysical surveys (from multibeam bathymetry and high-frequency seismic reflection data).
2. Assessment of the recent activity of the Iznik Fault, based on multiproxy analysis of sediment cores from each side of the fault.
3. Evidence for the timing of the last rupture corresponding to the 1065 CE historical earthquake, which had significantly impacted the city of Iznik.

Abstract

The seismic activity of the middle strand of the North Anatolian Fault (MNAF), Northwestern Turkey, is debated because of its quiescence during the instrumental period, in contrast to a significant historical activity documented by several chronicles over the last two millennia. Here, we focus on Lake Iznik, bordered by the MNAF, to get a new insight into its long-term seismicity and its tectonic setting. The study of lacustrine sediment cores reveals fourteen earthquake-induced turbidite deposits since their ages correspond to seismic events during the past two millennia. Bathymetry and high-resolution seismic reflection data allow to describe two hitherto unknown subaquatic active fault structures (the Boyalica and Iznik faults) that belong to the MNAF system. Sediment cores sampled on both sides of the Iznik Fault document an event deposit and a sedimentary unit vertically offset of ~50 cm interpreted as the last rupture during the 1065 CE destructive earthquake. Older events are supposed on this fault more than thousand years ago. Further studies will help to estimate the horizontal coseismic offset of this oblique-slip fault and the calendar of older ruptures. The current seismic gap of thousand years on this segment greatly increases the seismic hazard in this region and must be considered in the seismic risk assessment of the NAF system.

Plain Language Summary

During large earthquakes, sediments are generally transported from lake slopes to the lake basin. The resulting event deposits can provide information on the recurrence of past regional earthquakes, which is crucial for seismic hazard assessment. In this study, we discovered two underwater fault structures in Lake Iznik, using geophysical methods. Studying the sedimentation on both sides of the southernmost fault, we observed an increased sedimentation rate on the hanging wall of the fault immediately after an event deposit, dated at 1096 +/- 86 cal. CE. We interpreted these indicators as resulting from a coseismic vertical displacement along the fault plane, corresponding to the 1065 CE earthquake, which had significantly impacted the city of Iznik. We also show that most of the other event deposits in the sediment cores are confidently associated to 14 historical earthquakes.

Keywords: North Anatolian Fault, Lake sediment, Fault activity, Earthquake, Turbidite, paleo-seismicity.

1. Introduction

Earthquakes are the costliest and deadliest natural events in Turkey with about 100,000 deaths in the last century (Öcal, 2019). Despite their lower frequency compared to other events such as floods, the impact of earthquakes cannot be ignored in this densely populated part of the world. The seismic hazard in the northwestern part of Turkey is mainly linked to the North Anatolian Fault (NAF), a 1500 km-long right-lateral strike-slip fault, which accommodates the westward migration of the Anatolian microplate, away from the Eurasian/Arabian collision (Reilinger et al., 2006).

In its western termination, the NAF zone displays a complex organization as it is divided into three branches (*Fig.* 1). Its northern strand (NNAF) continues south of Istanbul through the Marmara Sea (e.g. Armijo et al., 2005). Its middle strand (MNAF) borders the south of two successive basins, known as the Geyve-Pamukova Basin and the Iznik Basin, which hosts Lake Iznik and continues through the Gemlik Bay to the southern shore of the Marmara Sea (*Fig.* 1). Its southern strand (SNAF) is less pronounced in the landscape and extends across the Bursa Province (*Fig.* 1). With a relative horizontal motion estimated around 5 mm/yr by GPS (Ergintav et al., 2014), both MNAF and SNAF show a deformation rate 5-fold smaller than the NNAF (~ 25 mm/yr) (Reilinger et al., 2006). This is also reflected by the recent seismicity of the NAF: from 1939 to 1999, a sequence of great earthquakes (moment magnitude Mw > 6.8) shifted westward from Erzincan to Düzce and Izmit (*Fig.* 1; Stein et al., 1997). The last major earthquake on the NNAF occurred in 1999 along the Izmit-Sapanca rupture and was a 7.6 Mw event. A ground-motion study revealed that this fault segment broke with a supershear velocity during the earthquake (Bouchon, 2002). This destructive event caused extensive liquefaction-induced ground deformation on the shores of Lake Sapanca triggering the submergence of a hotel (Cetin et al., 2002). The succession of the earthquakes on the NNAF is explained by the cumulative Coulomb stress along the fault (Stein et al., 1997). According to this concept, a seismic gap is inferred on the NNAF segment in the Marmara Sea, which was seismically inactive since the 18th century (Hubert-Ferrari et al., 2000). This future rupture may lead to a Mw > 7 earthquake and strike Istanbul (Parsons, 2000; Armijo et al., 2005). However, these different models only encompass the recent seismicity (since 1700 CE) on the NNAF branch, but do not take into account either the MNAF or the SNAF. While the SNAF produced a 7.3 Mw earthquake in 1953 and a 6.9 Mw earthquake in 1964 (Ambraseys, 2002), no major earthquake ruptured on the MNAF for several centuries, and a very low seismicity has been recorded during the instrumental period. These observations have led to

the assumption that this branch possibly became deactivated (Le Pichon et al., 2014). The last big earthquake on the MNAF may have occurred between the 14th and 18th centuries CE (Ambraseys, 2002). This long quiescence strongly contrasts with a significant historical tectonic activity on the MNAF. Several chronicles and archaeological studies report the partial destruction of Iznik (previously called Nicaea) and surrounding cities following ~ 15 major earthquakes within the last 2000 years, without any precision on the rupture segments (Ambraseys & Finkel, 1991; Ambraseys & Jackson, 2000; Ambraseys, 2002; Benjelloun, 2017). The quiescence of the MNAF in recent times may hide a longer seismic recurrence, which possibly is just as hazardous as the NNAF (according to their span of quiescence), but has been underestimated by the models. This study aims to precise the calendar of seismicity on the area of Iznik and to provide new data for the tectonic setting of the MNAF to precise the seismic cycle of this fault strand.

Lake sediments are continuous archives used to reconstruct past earthquake history (Monecke et al., 2004; Strasser et al., 2006; Christian Beck, 2009; Strasser et al., 2013; Van Daele et al., 2015; Avşar et al., 2015; Wilhelm et al., 2016; Moernaut et al., 2017; Rapuc et al., 2018). Compared to historical and terrestrial archives, lake sediments provide a complementary and more continuous paleoseismic record (e.g. Strasser et al., 2013; Wilhelm et al., 2016). Combining on-fault studies such as trenching with studies investigating earthquake-induced turbidites in lakes not only provide direct evidence for fault displacement in the case of surface ruptures, but also allows to document seismic events off-fault without surface ruptures (Brocard et al., 2016). We propose here to investigate Lake Iznik associating geophysical and sedimentological approach to provide new insights into the seismicity of the Iznik region over the past millennia. These methods have been already used on submarine ocean-floor faults such as in the Marmara Sea or in the Lesser Antilles (Armijo et al., 2005; Beck et al., 2012).

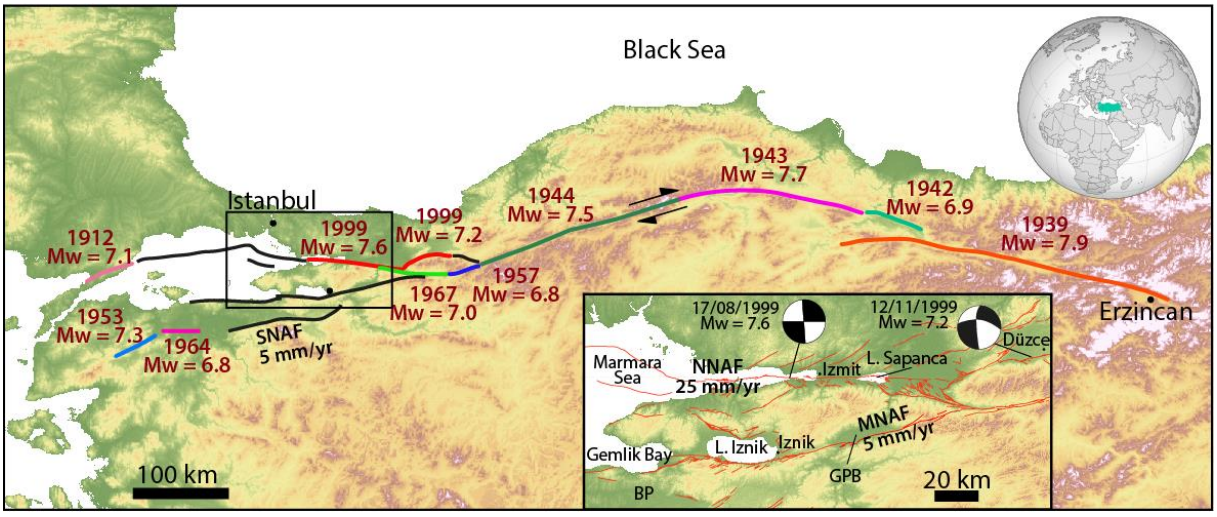

*Fig. 1: Shuttle Radar Topography Mission (SRTM - 1 arc-second resolution; https://earthexplorer.usgs.gov/) digital elevation model (DEM) with the different fault strands which ruptured during the major earthquakes of the 20*th *century (respective age, location and moment magnitudes indicated from USGS earthquake catalog;* https://earthquake.usgs.gov/earthquakes/search/ *and Stein et al., (1997)). The seismic gaps at the western termination of the NAF are underlined (black lines). Inset is a zoom of the studied part with the different strands of the NAF. GPB refers to the Geyve-Pamukova Basin, BP to the Bursa Province. Focal mechanism solutions are retrieved from Tibi et al., (2001). Active faults are shown in red (Benjelloun, 2017; Emre et al., 2018).*

2. Context

2.1 Geological settings and previous studies on the MNAF

The NAF was initiated some 11-13 Ma ago within a wider pre-existing shear zone, which became progressively narrower through time (Şengör et al., 2014). While most of NAF segments show right-lateral kinematics, the MNAF and the SNAF show oblique (transtensional) kinematics, with local deformation partitioning between right-lateral strike-slip and extensional regimes (Doğan et al., 2015; *Fig. 2*). The origin of the Iznik Basin is still under debate: it has been interpreted as a superimposed basin evolved due to the intersection of the younger NAF and the Thrace Eskişehir Fault (Yaltırak, 2002; Öztürk et al., 2009) or as a more complex transtensional basin due to MNAF activity (Doğan et al., 2015). The geological inheritance is reflected by the relatively high lithological heterogeneity and tectonic complexity within the watershed (*Fig.* 2a). The Gürle Fault (a segment of the MNAF) is known to have an normal component (Doğan et al., 2015), which explains the current location of the deepest depocentre of Lake Iznik (~ 75 m depth b.l.l.; *Fig.* 2a). This normal component is also expressed by the 100 m-high triangular facets on Lake Iznik's southern shore (*Fig.* 2b). Fault partitioning certainly exists; whereas the onshore Gürle Fault accommodates most of the normal component, another fault segment should somewhere accommodate the dextral component.

At least fifteen destructive earthquakes were recorded in historic chronicles during the last two millennia (Ambraseys & Finkel, 1991; Ambraseys & Jackson, 2000; Ambraseys, 2002; Benjelloun, 2017). More than 20 trenches carried out on different faults of the MNAF confirmed the fault activity (e.g. Honkura & Işikara, 1991; Barka, 1993; Uçarkuş, 2002; Doğan, 2010; Özalp et al., 2013; see *Fig. 2*a for their locations),

but very few of them gave reliable age. It is therefore difficult to conclude on the precise ages of rupture on the different segments of the MNAF, and on their earthquake recurrence rate. The city of Iznik hosts many archeological remains affected by past earthquake occurrences, such as the recently discovered submerged basilica in Lake Iznik (Şahin, 2014; Şahin & Fairchild, 2018). Through a systematic survey of Earthquake Archeological Effects (EAE) on Iznik's buildings, Benjelloun (2017) showed that three damage episodes are recorded: between the 6th and late 8th centuries CE, between the 9th and late 11th centuries CE and after the late 14th century CE. The second episode is clearly related to an earthquake in 1065 CE that was well described in many local chronicles and caused several damages in Iznik, whereas the two other episodes could be explained by different earthquake scenarios.

2.2 Lake catchment

Lake Iznik (83.5 m a.s.l, 40°26'N, 29°32'E), formerly known as Lake Askania, is located southeast of the Marmara Region (Bursa Province), east of the Gemlik Bay (*Fig.* 1). It is the fifth-largest lake of Turkey, and the largest of the Marmara Region with a N-S and E-W extent of 12 and 32 km, respectively (*Fig. 2*a). The lake has a catchment area of ~1257 km² and a surface area of 313 km². The watershed shows a heterogeneous geology, with a northern part relatively rich in volcanic, metamorphic rocks and carbonates, while the southern part is mostly composed of siliciclastic sediments with only sporadic carbonate and volcanic sections. Iznik has been an important city throughout history. Different archaeological excavations in the area suggest that the first farming activities began 6000-5400 BCE (Roodenberg, 2013). Since the first humans settled in the watershed, the land has been cultivated: cereals, olives, and walnuts were among the most important crops in the Iznik area (Miebach et al., 2016). The lake is peanut-shaped with a non-regular shoreline (*Fig. 2*a). A rough bathymetry of the lake, assembled by the General Directorate of Turkish Hydraulic Works (DSI), shows that the lake comprises three sub-basins, reflecting its tectonic complexity (*Fig.* 2a). One isolated sub-basin is located in the western part of the lake, whereas two sub-basins form the central and eastern parts, with one in the North and one on the South separated by an E-W elongated ridge (*Fig.* 2a). The main inflows are the Sölöz, Nadir, Kuru, Kara and Kiran rivers (*Fig.* 2a). The only outlet of the catchment is the Karsak River, which discharges the waters westward to the Marmara Sea through the Gemlik Bay. The Iznik Basin is bordered by two mountain ranges: the Samanli Mountains (max. elevation 1227 m a.s.l.) to the North, and the Katırli Mountains to the South (1275 m a.s.l.) (*Fig.* 2a). The study of Lake Iznik's sediments have provided an up to 36 kyr-long paleoclimatic

archive (Roeser et al., 2012; Ülgen et al., 2012; Viehberg et al., 2012; Miebach et al., 2016). In these past studies of Lake Iznik's sedimentary archives, no event deposits were identified in the sedimentary sequence.

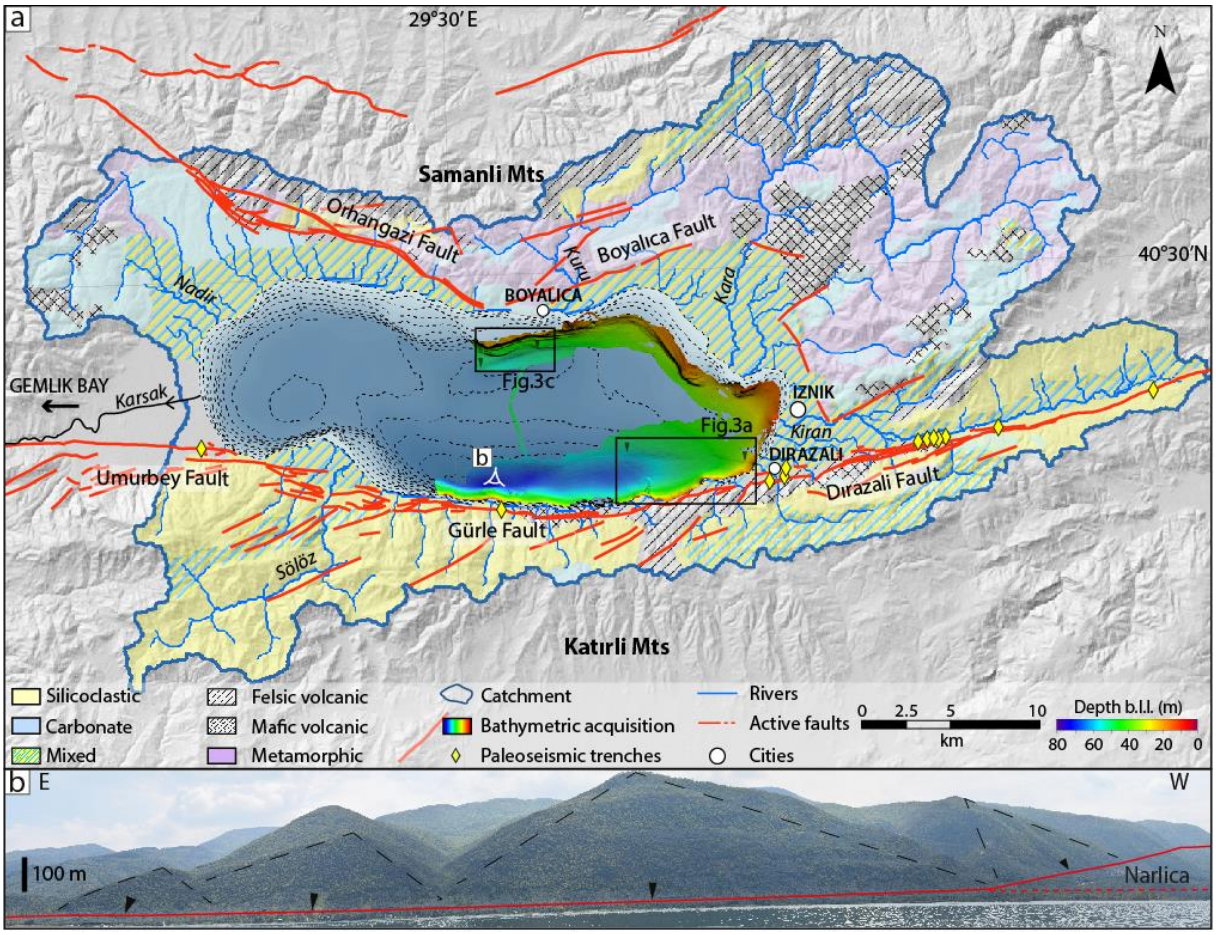

Fig. 2: (a) Lithological map of the watershed of Lake Iznik (modified from Viehberg et al., (2012)) and limits of its catchment (dark blue line). The hillshade relief is generated from the SRTM DEM (1 arc-second resolution). The main rivers are drawn in blue. The MNAF and other active faults are represented in red (Benjelloun, 2017; Emre et al., 2018). The bathymetric contour lines in the lake represent 5-meter intervals (DSI), superimposed by the hillshaded bathymetry acquired in this study (2 m grid), with a sun illumination angle/elevation of 20°N/45° respectively. A vertical exaggeration of 15 was applied. The color scale represents the depth below lake level (b.l.l.), based on a long-term reference lake level of 83.5 m above sea level. The black arrows show the visible extremities of the two newly discovered faults. The black rectangles indicate the location of Fig. 3a and c. (b) Photography of the southern shore of the lake taken from the lake and facing southward, showing triangular facets (black dashed lines) along the Gürle Fault (black arrows). These patterns highlight the significant normal tectonic component in this area.

3. Methodology

3.1 Bathymetry

The bathymetric survey was completed in April 2019 using a fishing boat with a Kongsberg EM2040 multibeam echosounder (Kongsberg Maritime, Horten, Norway, provided by University of Bern) in a single-head configuration (1° by 1° beam width, 300 kHz standard operating frequency; 400 depth detections per ping). The angular coverage was 148° maximum, with a coverage of up to ~3 times water depth on a flat bottom. The transducers and auxiliary sensors Kongsberg Seatex MRU5+ motion sensor (Kongsberg Seatex, Trondheim, Norway), a Trimble SPS361 heading sensor (Trimble Navigation Limited, Sunnyvale, CA, USA), a Leica GX1230 GNSS receiver (Leica Geosystems, Heerbrugg, Switzerland) using the TUSAGA Aktif GEO real-time positioning service (national active fixed GNSS, Turkey; typical position accuracy 2 to 3 cm) and a Valeport MiniSVS sound velocity sensor (Valeport Limited, Totnes, UK) were used. The transducers, motion sensor and mini sound velocity sensor were incorporated in a rigid mounting attached to the bow of the ship. The ship speed ranged from 7-9 km/h.

The vertical sound velocity in the water column was recorded daily by a Valeport Sound Velocity Profiler (SVP) that recorded pressure, temperature and the sound velocity in the water column. Sound velocity depends on the temperature and the salinity of the water. The absolute depth accuracy depends on the correctness of the water velocity profiles, the motion sensor's capability to compensate for ship movements due to waves, positioning accuracy, the water depth and is in the range of centimeters (shallow waters) to a few decimeters (>50 m depth). Data were recorded using Kongsberg's SIS software and processed in HIPS/SIPS 10.4.13 software (University of Bern), then interpreted using ArcGIS 10.4.1.

3.2 Seismic acquisition

The seismic profiles were acquired using a 3.5 kHz system (Geopulse, Geoacoustic) in 2005 with a single-channel streamer (20-elements AE5000, GeoAcoustics) and an array of four sub-bottom profiling transducers (Mod. TR-1075A, Massa, USA) as receivers. Shot interval was 1 second. For navigation, a 3x4 m UWITEC aluminum platform ("R/V Helga") equipped with 4 inflatable tubes for flotation and a 25 HP outboard engine were used. The average speed of the vessel was 5 km/h. All 3.5 kHz data were digitized (Octopus 360, Octopus Marine Systems, UK) and processed (15 to 5000 Hz filtering) using Reflex

software (Sandmeier Software, Germany). All profiles were interpreted using IHS Markit® Kingdom v.2015.

3.3 Coring and lithological description

Five short cores (registered in the French national cyber-core-repository https://www.cybercarotheque.fr and the open international database www.geosamples.org as IZN19_03 (1.37 m; IGSN: **pending**), IZN19_04 (1.60 m; IGSN: **pending**), IZN19_16 (1.25 m; IGSN: **pending**), IZN19_21 (2.70 m; IGSN: **pending**) and IZN19_31 (2.79 m; IGSN: **pending**)) were collected from Lake Iznik in April and July, 2019, using a UWITEC gravity corer with hammering. The cores were sampled on strategic points, depending on the first bathymetric and seismic results. In the laboratory, the cores were split into two halves. Each core was photographed after oxidation and a detailed sedimentological description was performed. The lithological description of the sequences allowed the identification of different sedimentary structures and facies, which were then correlated between the cores. Colors were assigned according the Munsell's color chart (Munsell Color, 1994).

3.4 Sedimentological analysis

Grain-size analysis

The grain-size distribution of the sediment was determined following a mean of 5 cm sampling step all along the longest sequence (IZN19_21; *Fig. 3* for location). As the sequence contains sporadic mm-thick sandy deposits, the resolution in these parts was increased to 0.5 cm. A Beckman Coulter Life Science 13 230 XR laser particle-size analyzer was used (EDYTEM Laboratory, University Savoie Mont Blanc) with sonication to avoid particle flocculation. Two runs with a 30s-long measurement were applied for each fresh sample. Results of the grain-size distribution were processed with MATLAB R2016b software and presented in a contour plot with a color-scale according to the abundance of particles in percentage for each grain-size class (*Fig. 5*a).

Scanning Electron Microscopy (SEM) and Energy-Dispersive Spectroscopy (EDS)

To complete the core description, a representative 8 cm-long slab including two coarser-grained deposits was resin-embedded to make 1 mm-thick thin sections of the sediment, which were analyzed with a Vega3 Tescan Scanning Electron Microscope (ISTerre Laboratory, University Grenoble Alpes) following covering with a graphite layer of 20 µm. Representative areas of the thin section were additionally analyzed

with an Energy-Dispersive Spectroscopy (EDS) probe (Rayspec with SamX's electronic system and software, ISTerre Laboratory) to examine the elementary composition and to map chemical elements on specific lamina.

Loss on ignition

The loss on ignition (LOI) analysis was performed on the IZN19_31 sequence (*Fig. 3* for location), with a 10-cm sampling interval all along the sequence to estimate organic matter (OM) and carbonate proportion in the sediment, following the protocol described by Heiri et al., (2001).

3.5 Geochemistry

The relative contents of major and trace elements were analyzed with an X-Ray Fluorescence (XRF) at 1-mm resolution on the surface of each sediment core with an Avaatech Core Scanner (EDYTEM Laboratory). The split core surface was first covered with a 4-µm-thick Ultralene film to avoid contamination and desiccation of the sediment. Element intensities are expressed in counts per second (cps). Different settings were used with 10 kV and 0.2 mA during 15 s to detect Al, Si, S, K, Ca, Ti. and at 30 kV and 0.3 mA during 20 s for Mn, Fe, Ni, Cu, Zn, Br, Rb, Sr, Zr, Pb (Richter et al., 2006). A Principal Component Analysis (PCA) was performed on the geochemical results using R software version 3.5.1 (R Core Team, 2018) to determine correlations between the different measured elements and to identify principal sediment end-members, which are used to better constrain each sedimentological facies (e.g. Sabatier et al., 2010).

3.6 Chronology of the cores

Eleven ^{14}C analyses of eleven organic plant macro remains were performed by accelerator mass spectrometer (AMS) at the Poznan Radiocarbon Laboratory. The ^{14}C ages were calibrated using the Intcal13 calibration curve (Reimer et al., 2013). Calibrated ages are expressed in the Common Era (CE) timescale: years before the CE are denoted BCE (Table 1). The age model and the sedimentation rate were calculated using the R code package *clam* (Blaauw, 2010). The best fit was obtained by applying a smooth spline model with 0.44 for the smooth parameter.

4. Results

4.1 Lake Bathymetry

One third of the surface area of Lake Iznik (~ 80.5 km²), was mapped in high-resolution (*Fig. 2*a). Two prominent lineaments were discovered on the bathymetric data. One is located to the north, parallel to the onshore Boyalıca Fault and strikes NE-SW. This lineament separate the northern sub-basin and the shoreward underwater terraces (*Fig. 3*c).

The other lineament, striking NW-SE, has been discovered on the southeastern part and mapped over a distance of 9 km (*Fig.* 3a). It separates the southern sub-basin from the central ridge (*Fig. 2*) in the middle of the lake. This lineament presents two kinks separating it into three segments: IFS1, IFS2 and IFS3 (*Fig.* 3a*)*. IFS1 and IFS3 are ~3 km length (*Fig.* 3a). The bathymetric profile perpendicular to the IFS1 shows a ~1 m vertical offset of the lake floor (profile P1; *Fig.* 3d), extending over a distance of ~100 m. These segments are linked by IFS2 whose scarp is barely visible on the bathymetric data (*Fig.* 3a). Furthermore, numerous pockmarks are visible along the fault trace at the transition from IFS2 to IFS3, indicating fluid escapes (*Fig.* 3b). The size of these depressions varies from few centimeters to 6 m diameter and reaches ~60 cm deep (*Fig.* 3d). If the lineament extends ashore, it merges into the main branch of the MNAF, close to the village of Dırazali. However, the surface expression of the fault is masked by human activity, mainly due to fields of olive and fruit trees. According to these observations, we interpreted this lineament as a fault, termed Iznik Fault.

4.2 Seismic reflection data

High-resolution seismic profiles were acquired across IFS2 and IFS3 (*Fig. 3*a). These single-channel reflection sections show maximum acoustic penetration of ~10 ms two-way travel time or ~7.5 m (assuming acoustic velocities of 1500 m/s), after which signals become weaker and difficult to interpret due to high gas content of the sediment. A mass-movement deposit indicating a slope failure at the location of IFS3 is visible on the seismic section (Profile P2; *Fig. 4*) supporting the fault nature of the lineament and its location. Although it is difficult to assess vertical offset on the different seismic profiles, the continuity of the seismic reflections is affected across the fault. The second seismic section parallel to IFS2 (Profile P3; *Fig. 4*), does not show any clear slope failure but only slight vertical offsets of the seismic reflections and a series of closely-spaced incipient faults displacing steeply the uppermost meters of sediment.

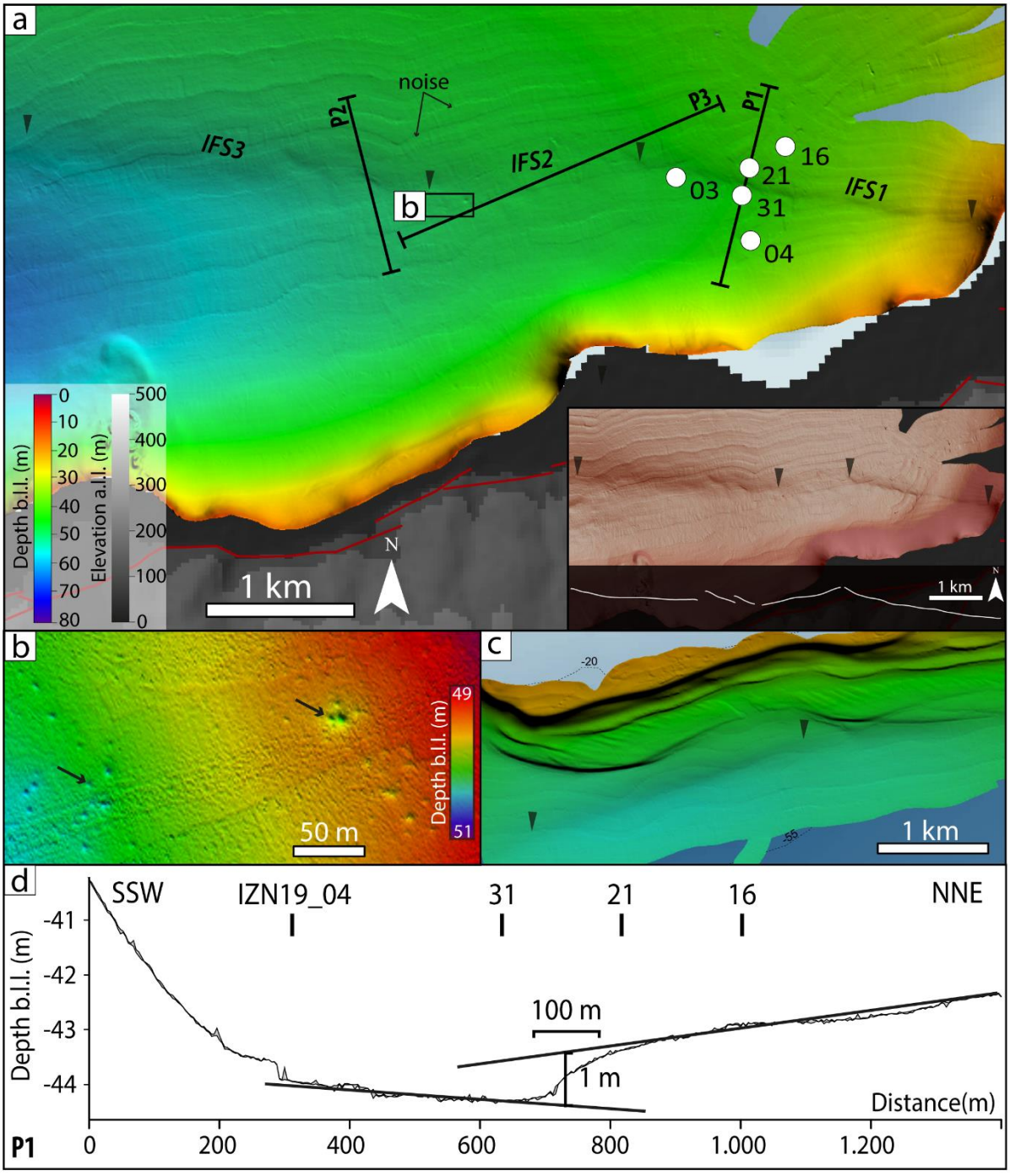

Fig. 3: (a) Hillshaded bathymetric map (5 m grid) of the southeastern part of the lake (Fig. 2 for location). A vertical exaggeration (ve = 20) is applied to highlight the Iznik Fault trace. The black arrows denote the extremities of the different visible segments of the Iznik Fault, termed as IFS1, IFS2 and IFS3 from east to west. White dots represent the core locations (IZN19_03, 04, 31, 21, 16). Black lines indicate topographic P1 (Fig. 3d) and seismic section locations (P2 and P3; Fig. 4). Subaerial elevation is derived from the SRTM model (1 arc-second resolution). The bathymetric and topographic scales are relative to the lake

level, below and above (denoted as b.l.l. and a.l.l, respectively). Active faults ashore are shown in red (Benjelloun, 2017; Emre et al., 2018). Inset is an overlay of hillshade and slope maps to emphasize the fault traces. Black arrows indicated the termination of IFS1 and IFS3. In the lower part, an interpretative sketch of the fault geometry is shown. (b) Zoom of the pockmarks along the fault, indicating fluid escapes (1 m grid; ve = 10). Location is shown as a black rectangle in the main figure. (c) Hillshaded bathymetric map of the northern basin, showing the northern lineament, limited by the black arrows (5 m grid; ve = 10; Fig. 2 for location). (d) Topographic profile P1 derived from the bathymetric data, with a 2-m horizontal resolution and consists of two lines, the min-max values. Core locations are indicating above the profile (IZN19_04, 31, 21, 16). The fault is characterized by a ~1 m step on a ~100 m-wide area. Hillshaded maps (a, b, c) have a sun angle/elevation illumination of 20°N/45°. Ve increases the noise in the data especially the swath traces.

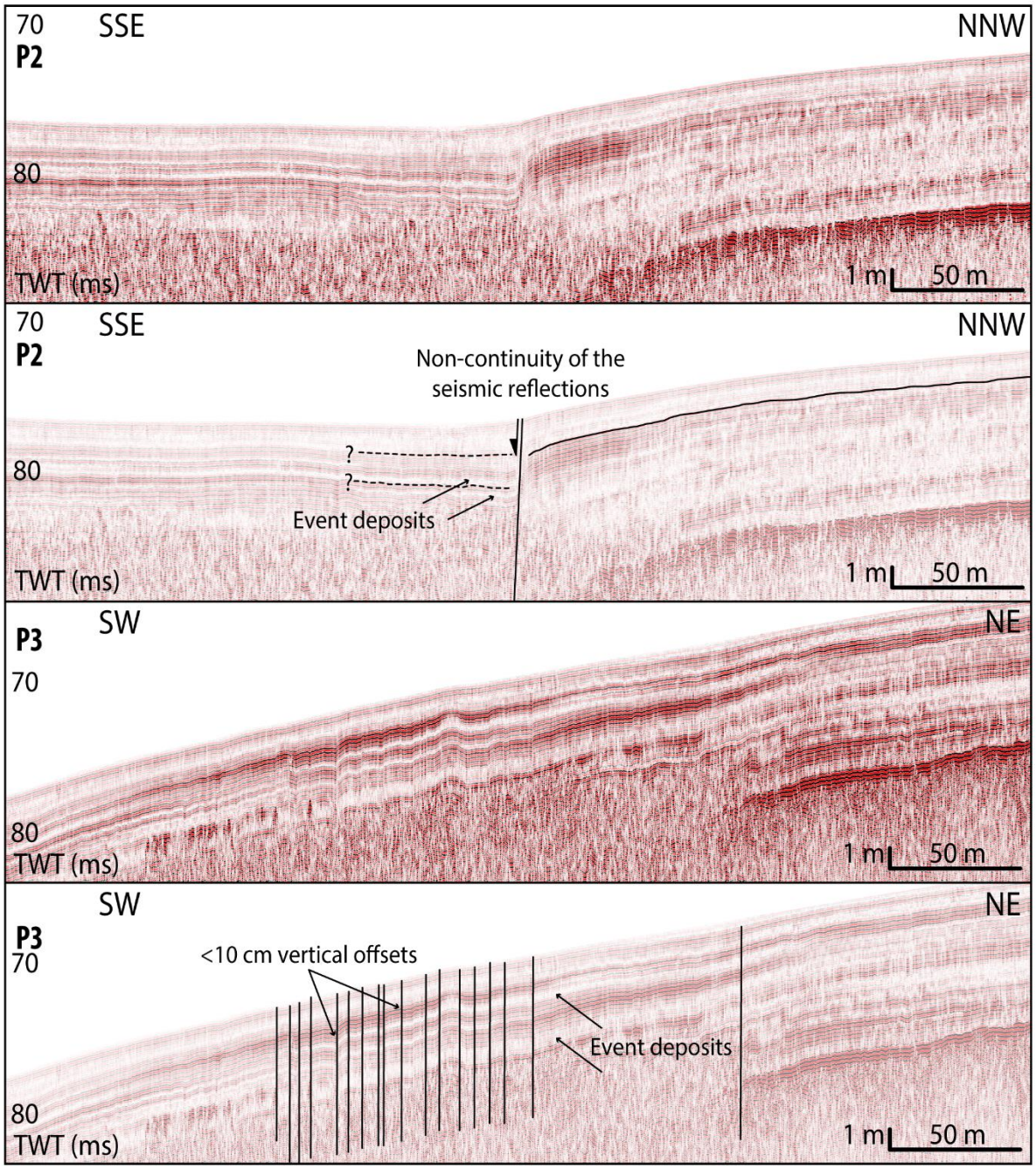

Fig. 4: 3.5 kHz single-channel pinger seismic profiles P2 and P3 (locations in Fig. 3a). A raw and an interpreted version is presented for each profile.

4.3 Sedimentary sequences

Sedimentary facies

Lake Iznik sediments consist mainly of clayey to silty grained (Roeser et al., 2012; *Fig.* 5). In the here investigated short cores, very fine to fine sand layers appear very sporadically at the millimeter scale in the finer matrix of background deposits. Based on macroscopic observations and confirmed by geochemical

311 analysis, four main lithologic facies were identified. Facies Ia is composed of brown (5Y/4/4) silty-clay
312 (D50 = 10 µm) and occurs at the top of each core. The organic proportion (LOI550) of this facies amounts
313 to ~9 % and the carbonate proportion (LOI950) to 6 %. Facies Ib occurs at different depths in the sequences
314 and consists of slightly coarser light brown (2.5Y/5/4) silt (D50 = 15 µm). Facies Ib has the highest
315 proportion of organic matter (~10 %) and carbonate (~10 %). The majority of the sedimentary sequence
316 consists of Facies II, which is a more heterogeneous facies with olive grey color (5Y/6/2) clay (D50 = 8
317 µm). This facies is interrupted by a total of 15 and 18 few-mm-thick (max 2 cm-thick) sandy layers in cores
318 IZN19_31 and IZN19_21, respectively, denoted as Facies III and termed 'event layers' (D50 = 20 µm). This
319 facies shows the lowest proportion in organic matter (~7 %) and carbonates (~7 %). Nevertheless, LOI
320 values do not vary much over the entire sequence. The fraction of non-carbonate ignition residue (NCIR) is
321 higher than 80 % for the whole sequence (*Fig.* 5a). All event layers appear to the naked eye as mm-thick
322 levels of very fine silt/sand or silty lenses within the continuous sedimentation of Facies II. The detailed
323 SEM observations show that these sandy layers have an erosive base incising into clayey sediments and a
324 fining-upward trend. Bioturbation with vertical burrows is present throughout their base. Burrow length
325 varies from 1 to 4 mm, and they are filled with particles to the overlying layer (*Fig.* 5c). Moreover, a
326 comparison of the oxide composition of two event deposits compared to the background sedimentation has
327 been performed with the EDS sensor (*Fig. 5*c). These maps show that Facies II and III have the same major
328 element compositions and that all carbonates within the Facies III are mostly composed by Ca and Mg and
329 reach 50 µm (*Fig.* 5c). Facies III layers are distinct from Facies II due to their fining-upward trends, their
330 erosive base and the coarse-grained Ca/Mg-carbonates (*Fig.* 5).

331 **Geochemistry**

332 PCA was conducted on the XRF geochemical data of both IZN19_31 and IZN19_21 cores located on both
333 sides of the fault (*Fig.* 5b). Dimensions 1 and 2 (denoted as Dim 1 and Dim 2) explain 85.17% and 80.12%
334 of the total variability for IZN19_31 and IZN19_21 cores, respectively. From the variables factor map, two
335 end-members could be identified. The first one, denoted as "terrigenous", shows high positive loadings
336 with Dim 1 (e.g. Al, Si, Ti, K, Rb; in green in *Fig.* 5a and b). The second end-member is interpreted as "in-
337 lake processes" (Ca, Sr, Br). It displays negative loadings on Dim 1 and positive loadings on Dim 2 (red in
338 *Fig.* 5a and b). We link it to the endogenic carbonate production and organic matter (Guevara et al., 2019).
339 The individual factor map highlights the characteristics of each facies. Facies Ib is dominated by the

endogenic process end-member, and it is also characterized by high Ca, Sr and Br counts (*Fig.* 5b). In contrast, Facies II is influenced by terrigenous input. Facies Ia is in an intermediate position with relatively higher Ti counts than Facies Ib (*Fig.* 5a). Facies III shows a similar geochemical characteristic as Facies II (*Fig.* 5c).

Core-to-core correlation

On the basis of the lithological description and XRF measurements, a correlation between the cores across the Iznik Fault is proposed (*Fig. 3*a and *Fig. 6*). The IZN19_03 Core has been excluded from the comparison to limit uncertainties because of its distance to this transect (IZN19_03 Core is presented Figure S1 in the supporting information). On *Fig. 6,* the Dim 1 (terrigenous supply vs. in-lake processes) and the Ca signal are displayed to highlight the stratigraphic units correlation. Five different stratigraphic units (from top to bottom: purple, green, orange, dark blue, grey) were correlated on the P1 profile across IFS1 (*Fig. 3*d). Thickness of these units varies significantly, particularly between cores in the immediate vicinity of the fault, IZN19_31 on the hanging wall and IZN19_21 on the footwall of the fault. Based on the stratigraphic correlation, it was possible to correlate the radiocarbon dates (*Table 1*) to IZN19_21 and IZN19_31 cores and use all of them for age modeling.

Fig. 5 (next page): Main sedimentological and geochemical results of IZN19_31 and IZN19_21 cores. (a) Macroscopic description, photography, XRF data (Ti, Ca, Sr, Ca/Sr and Ti/Ca). Ia, Ib, II denote the different facies types, sandy event layers (Facies III) are displayed in red. Cl, St, Sd and Pb abbreviations refer to the grain size observations: clay, silt, sand and pebble respectively. The LOI results are presented for the Core IZN19_31 while the grain-size contour plot is displayed for the Core IZN19_21 (b) PCA for cores IZN19_31 and IZN19_21. The respective variables factor maps show that two end-members are defined, one representing the in-lake processes and one corresponding to the terrigenous inputs. The individual factor maps show the correlations of each facies type with the different end members. (c) Detailed coupled SEM/EDS analysis of Facies II versus Facies III. Optical and SEM photos (left), geochemical mapping (right) show the relative abundance of major elements (Si, Ca, Mg) within the area studied (white box on the SEM photography). The relative oxide compositions between Facies II and III are shown below.

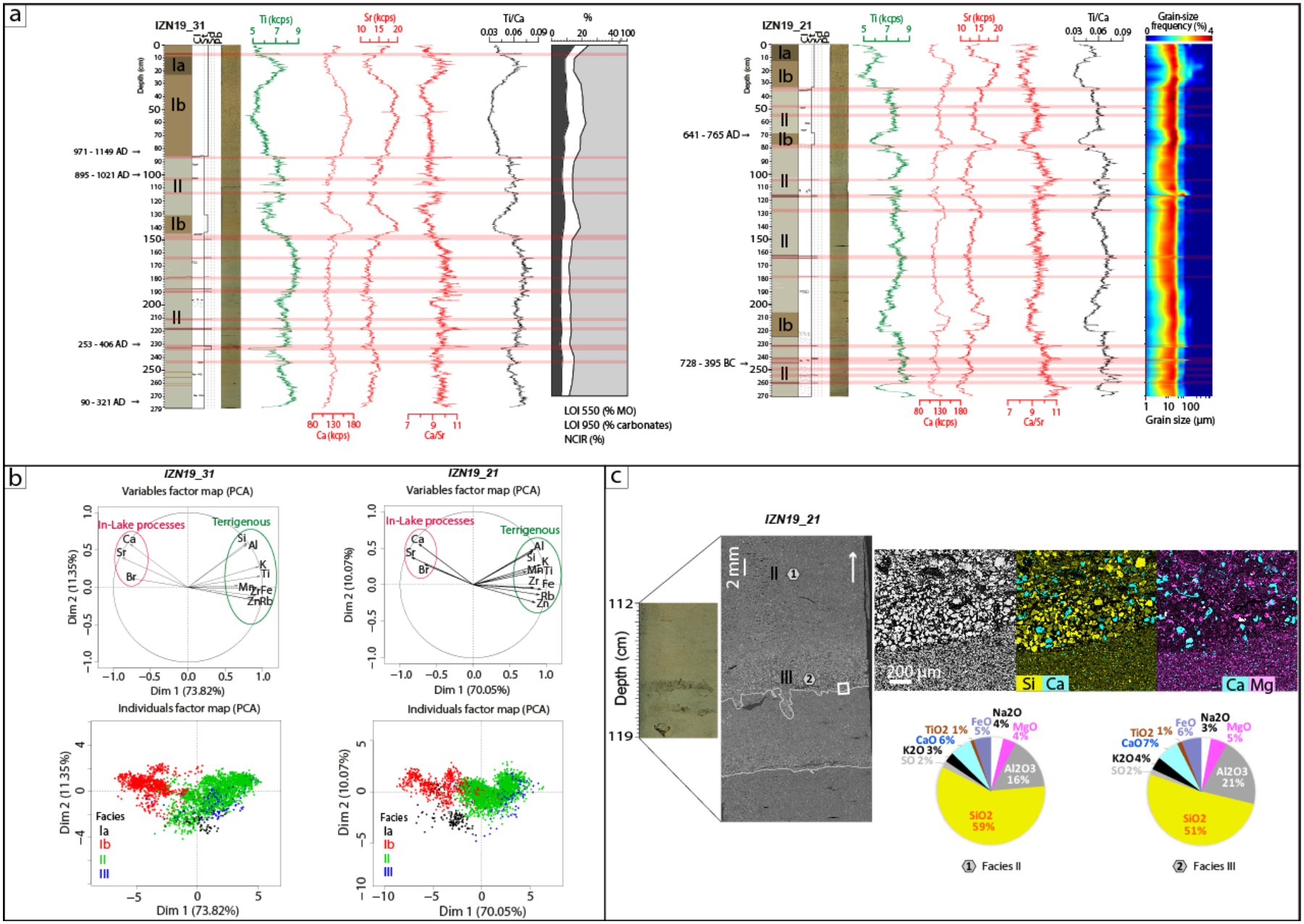
a
IZN19_31
Ti (kcps)
Sr (kcps)
Ti/Ca
%
Depth (cm)
Ia
Ib
II
Ib
II
Ib
II
971 - 1149 AD
895 - 1021 AD
253 - 406 AD
90 - 321 AD
Ca (kcps)
Ca/Sr
LOI 550 (% MO)
LOI 950 (% carbonates)
NCIR (%)
IZN19_21
Grain-size frequency (%)
Ia
Ib
II
Ib
II
Ib
II
641 - 765 AD
728 - 395 BC
Grain size (µm)
b
IZN19_31
Variables factor map (PCA)
In-Lake processes
Terrigenous
Ca
Sr
Br
Si
Al
K
Ti
Mn
Fe
Zr
Rb
Dim 2 (11.35%)
Dim 1 (73.82%)
Individuals factor map (PCA)
Facies
Ia
Ib
II
III
IZN19_21
Variables factor map (PCA)
In-Lake processes
Terrigenous
Ca
Sr
Br
Al
Si
K
MnTi
Zr
Fe
Rb
Zn
Dim 2 (10.07%)
Dim 1 (70.05%)
Individuals factor map (PCA)
Facies
Ia
Ib
II
III
c
IZN19_21
2 mm
Depth (cm)
112
119
200 µm
Si Ca
Ca Mg
Na2O 4%
MgO 4%
FeO 5%
TiO2 1%
CaO 6%
K2O 3%
SO 2%
Al2O3 16%
SiO2 59%
Facies II
Na2O 3%
MgO 5%
FeO 6%
TiO2 1%
CaO7%
K2O4%
SO2%
Al2O3 21%
SiO2 51%
Facies III

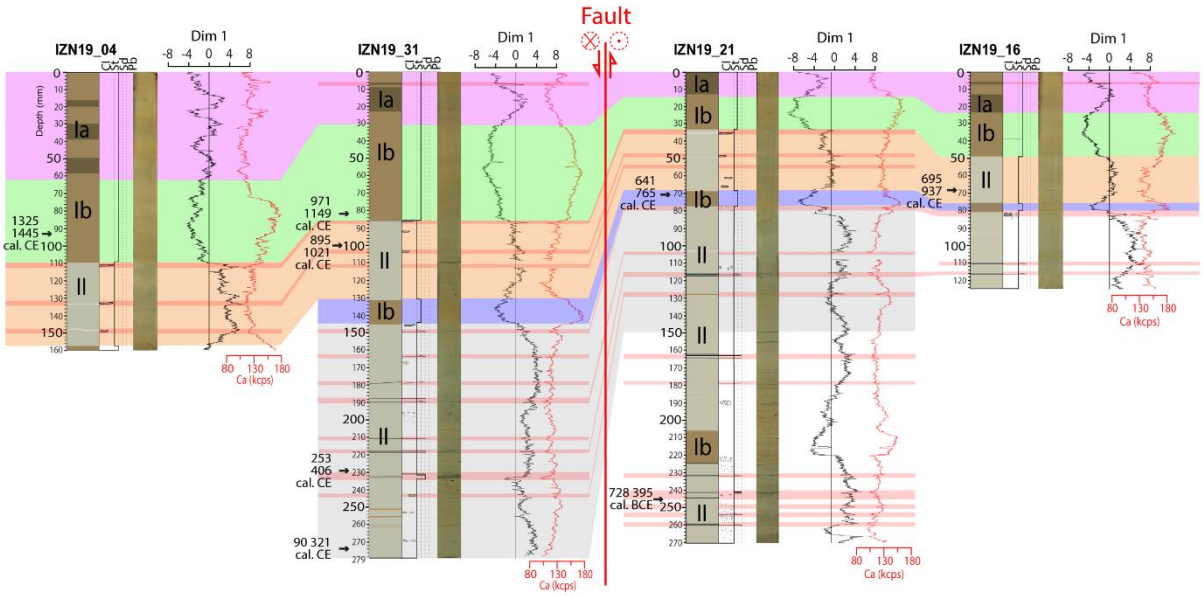

Fig. 6: Core-to-core correlation of the transect across IFS1 (Fig. 3a). Topography is neglected. For each core: lithological description, photography, Dim 1 and Ca signal are displayed. The different colors represent five stratigraphic units. Event deposits are shown in red. Individual radiocarbon dates are shown with black arrows (Table 1 for details). Ia, Ib, II represent the names of the different facies types defined in the text.

4.4 Radiocarbon dating and age models

Eleven organic terrestrial plant macroremains were dated (*Table 1*) and stratigraphically correlated between cores IZN19_31 and IZN19_21. This allowed us to use all dates on both cores for age modeling (*Fig. 7*). Both cores have almost the same length (279 cm and 270 cm, respectively) and they were taken very close one to the other (200 m apart) on each side of the fault. The core located north of the fault (IZN19_21) spans a larger period of time and reach at the base 625 cal. BCE, whereas the core south of the fault (IZN19_31) encompasses a shorter time period with the base reaching ~170 cal. CE. These different basal ages clearly document the higher sedimentation rates south of the faults. Core IZN19_31 shows more pronounced variations in the sedimentation rate, and four periods can be differentiated (*Fig. 7*). (1) a period with a relatively high sedimentation rate from 175 to 400 cal. CE. During this period, the sedimentation rate is almost constant (~2.4 mm/yr); (2) The sedimentation rate show a significant increase from 400 to 600 cal. CE reaching 4.7 mm/yr; (3) The sedimentation rate decrease and become stabilized at 0.8 mm/yr around 1200 cal. CE; and (4) Sedimentation rate increases from 1200 cal. CE until the modern period (1.2

388 mm/yr at the top). Core IZN19_21 shows the same trends but with less pronounced variations lacking also
389 the most recent increase in recent times (*Fig. 7*).
390

Sample name	**Core**	**MCD (cm)**	**Radiocarbon age (yr BP)**	**Age cal BCE/CE 2σ range**	**Sample type**
IZN19_20	IZN19_03	68	1170 +/- 35	770 – 969 CE	Plant remains
IZN19_21	IZN19_03	122.5	1555 +/- 30	421 – 570 CE	Plant remains
IZN19_22	**IZN19_03**	**136**	**1460 +/- 230**	**65 – 1022 CE**	**Plant remains**
IZN19_23	IZN19_16	68.3	1205 +/- 30	695 – 937 CE	Plant remains
IZN19_24	IZN19_21	70.5	1345 +/- 30	641 – 765 CE	Plant remains
IZN19_25	IZN19_21	245.5	2385 +/- 30	395 – 728 BCE	Plant remains
IZN19_42	IZN19_31	82.7	1015 +/- 30	971 – 1149 CE	Plant remains
IZN19_43	IZN19_31	97.8	1070 +/- 30	895 – 1021 CE	Plant remains
IZN19_44	IZN19_31	229	1700 +/- 30	253 – 406 CE	Plant remains
IZN19_45	IZN19_31	273.5	1820 +/- 30	90 – 321 CE	Plant remains
IZN19_49	IZN19_04	93	515 +/- 30	1325 – 1445 CE	Plant remains

391 *Table 1: Radiocarbon ages for the Lake Iznik sediment cores, in bold the rejected age for age model*
392 *computation. BP denotes Before Present, i.e. before 1950 CE. MCD denotes Meters Composite Depth.*

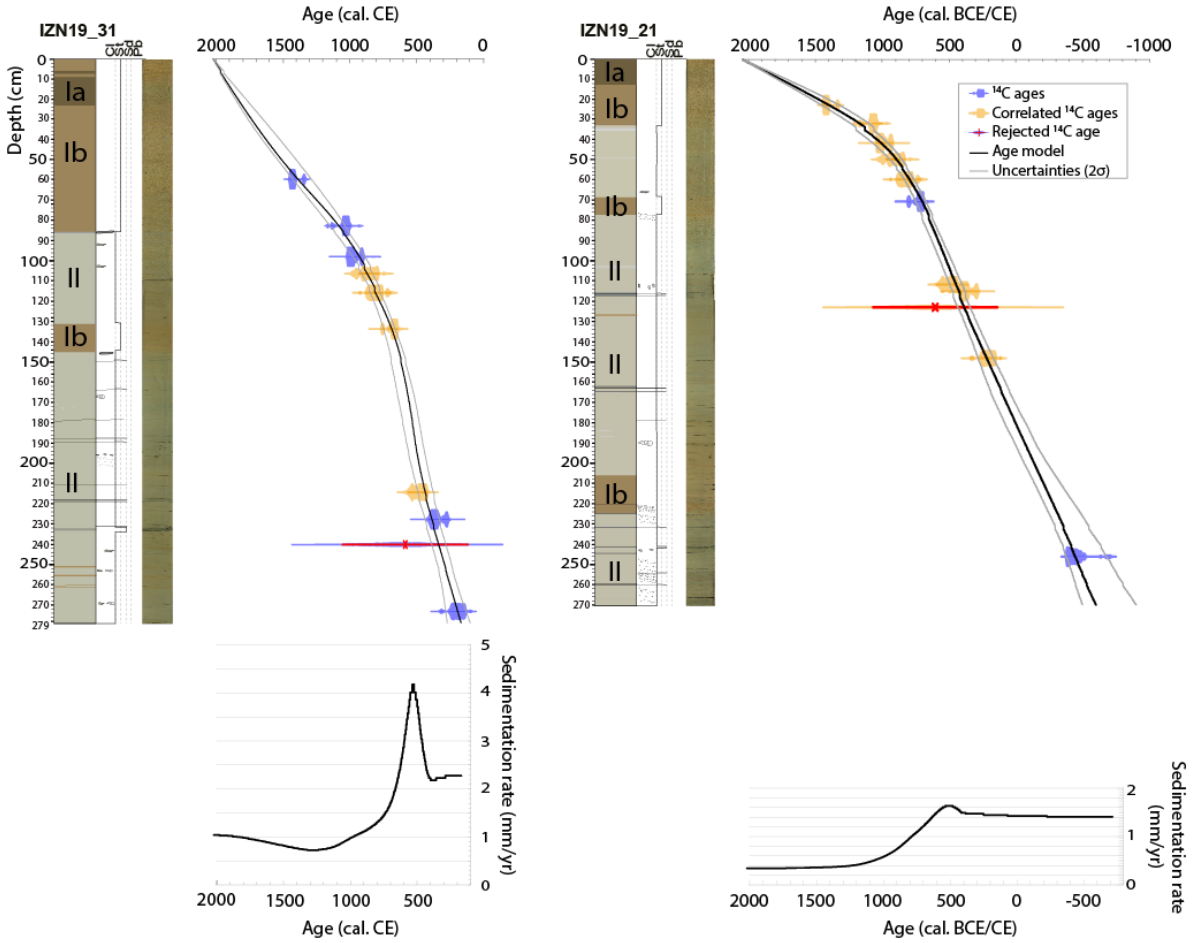

Fig. 7: Lithological description, photography, age model for cores IZN19_31 and IZN19_21 and their respective sedimentation rate variation curve through time. The age models are computed with Clam R package (Blaauw, 2010) *using the radiocarbon data (Table 1). The blue dates origin in the displayed core itself; the orange radiocarbon ages are those which are correlated from other sequences (Fig. 6). One radiocarbon age has been rejected for the age model computation due to its large uncertainty (marked in red, details in Table 1).*

5. Discussion

5.1 Event deposits versus seismic historical archives

The LOI analysis of the cores shows that almost 80% of the whole sediment sequences are composed of terrigenous siliciclastic constituents (*Fig. 5*a), whereas the in-lake carbonate production represents only a minor fraction. Roeser et al., (2016) showed that endogenic calcium carbonates precipitated as aragonite and low-Mg calcite in the lake water column. The terrigenous component is expressed in a high Ti counts,

406 which is characteristic of siliciclastic and felsic volcanic rocks in this part of the catchment (*Fig.* 2a; *Fig.*
407 *5*a, b). Our study reveals evidence for multiple thin Ti-rich sandy normally graded beds termed event layers
408 within Facies II (*Fig. 5*). These deposits show Ca and Sr negative counts excursions suggesting a decrease
409 in the proportion of endogenic carbonates (*Fig.* 5a, b). They are interpreted as turbidites because of: (1) the
410 macroscopic lithological and structural description; (2) their higher proportion in terrigenous elements as
411 indicated by the Ti/Ca ratio (*Fig.* 5a) and (3) their higher values of detrital carbonates shown by the Ca/Sr
412 ratio and the presence of Ca/Mg coarse-grained carbonates (*Fig.* 5a, c).
413 Turbidites can be triggered by several processes such as hyperpycnal flow related to river flooding (e.g.
414 Wilhelm et al., 2015), remobilization of superficial lacustrine slope sediments that have been transported
415 and deposited by turbidity currents (e.g. Hage et al., 2017), in relation to seismically induced massive
416 subaquatic failures of lateral slopes (e.g. Schnellmann et al., 2005) or spontaneous slope failure due to high
417 surcharge in sediments of submerged delta slopes (e.g. Girardclos et al., 2007; Hilbe & Anselmetti, 2014).
418 The last two are less probable as shown by the small slope in this area (less than 5°) (Schnellmann et al.,
419 2005). Turbidite deposits are getting thinner from SW to NE (*Fig.* 6) and some of these deposits are absent
420 in Core IZN19_16, which is farther away from the closest significantly sediment contributing delta (*Fig.*
421 3a). The frequency of these turbidites and in particular the fact that no deposit has been observed over the
422 last 1000 years is difficult to explain with the "flood hypothesis". However, given the active tectonic
423 context of the region, it is plausible that such turbidites are related to shallow slope destabilizations by
424 recurrent earthquakes, as previously proposed for thin turbidites in a similar context of Lake Hazar (~ 900
425 km southeastward; Hage et al., 2017; Hubert-Ferrari et al., 2020). To evaluate this potential seismic cause,
426 the age of the turbidites, deduced from age models of cores IZN19_21 and IZN19_31 are compared with
427 those of the historical earthquakes (Ambraseys & Finkel, 1991; Ambraseys & Jackson, 2000; Ambraseys,
428 2002; Guidoboni et al., 2005; Ambraseys, 2009; Table S1 in supporting information). The sensitivity of
429 Lake Iznik to record regional earthquakes can be characterized by the Earthquake-Sensitivity Threshold
430 Index (ESTI) (Wilhelm et al., 2016), for which the sedimentation rate is critical in controlling the ability of
431 a lake system to record earthquake-induced deposits: the higher the sedimentation rate is, the greater the
432 ESTI and the more likely it is to record earthquakes. As the sedimentation rate changes through time (*Fig.*
433 7), the ESTI of Lake Iznik also changed accordingly. A weighting of earthquake magnitudes by the

sedimentation rate over 100 years prior to the event is performed, thus the relationship between the sedimentation rate and the turbidites occurrence is explored in *Fig. 8*.

In Core IZN19_21 that spans a longer time period till 625 cal BCE, eighteen distinct event deposits are observed. Six of them are older than 0 cal CE; thus predate the first historical seismicity records for this area. For the twelve remaining sandy layers, eleven historical earthquakes can be related to turbidite deposits (*Fig. 8*e, f). The last event layer is identified in the higher sedimentation rate period (450 to 600 cal CE) probably related to enhanced erosion by intense human activities during Roman time (Arnaud et al., 2016; Bajard et al., 2017) such as agriculture as reflected in high amounts of olive-tree pollens (Miebach et al., 2016). These fields were abandoned around 650 CE when Pinus pollen increased (Miebach et al., 2016). This rise in the sedimentation rate explains the increased sensitivity of the lake to record ground-shaking (Wilhelm et al., 2016; Rapuc et al., 2018). During such periods, the lake is prone to recorded earthquakes with significantly smaller magnitude, which might not be reported in historical accounts. We cannot exclude that the deposit could also be related to other triggering mechanism such as flood, considering that at least one flood is mentioned in a historical archive for that time period during the reign of Justinian (527-565 CE) (Evans, 2005).

In Core IZN19_31, fifteen event deposits are described, all of them in the time span of historical accounts. Eleven are associated with earthquakes. The four others also appear in the high sedimentation rate period during which the lake sensitivity was high. Overall, this approach shows conclusive results as twenty two thin turbidites can be associated with earthquakes in both cores, corresponding to fourteen independent earthquakes (*Fig. 8*). In turn, those historically known earthquakes that were not recorded by a turbidite are generally separated by only few years. As an example, two sandy layers visible in Core IZN19_31 at 232 cm depth (*Fig. 5*) are not present in the IZN19_21 sequence. Based on the age model (*Fig. 8*a), these turbidites could correspond to two of the three historical earthquakes known from that time: 358, 362 and 368 CE. According to *Fig. 8*c, the 358 and 362 CE earthquakes seem to be the most prone to be recorded in this part of the lake as they are further from the threshold. Hence, the 358 CE earthquake could have been recorded as a thick deposit (2 cm i.e. more than four times thicker than all other sandy layers), then the overlying thinnest coarse-grained layer probably corresponds to the 362 CE earthquake (*Fig.* 8c). The lack of a third layer marking the 368 CE earthquake thus likely indicates that the slopes did not have enough time to replenish the re-mobilizable sediment stock to form a new turbiditic deposit within only a few years

after two earlier earthquakes. Nevertheless, historical data (e.g. Guidoboni et al., 1994) indicate that Iznik was mostly destroyed during the earthquake of 368 CE, so that an alternative hypothesis relates the overlying deposit to this earthquake and uncertainties still remain for the assignments of historical events during this period. Furthermore, Iznik was highly damaged or destroyed by local events in 29 CE, 368 CE, 740 CE and 1065 CE with earthquake magnitudes estimated between 6.8 and 7.2 (Ambraseys, 2002). These magnitudes were calculated from the spatial distribution of intensities around the maximum intensity zone (Ambraseys, 2002), which in turn were estimated from historical accounts. However, variable population, changes in building vulnerability over time and exaggeration in the historical sources are difficulties affecting these estimations.

Considering the historical location and magnitude (Ms = 6.8) of the 1065 CE earthquake, it should not be recorded in our cores, when it is. Therefore, we should reconsider either the epicenter location or its magnitude.

Concerning the instrumental period, ~8500 earthquakes (from 1935 to 2020) are plotted (*Fig. 8*c, f). These earthquakes occurred in an area of 200 km around Lake Iznik and with magnitudes (magnitudes types depending on the earthquakes) ranging from 2.5 to 7.6 (USGS catalogue; https://earthquake.usgs.gov/earthquakes/search/). Among these earthquakes, only the 1999 CE event (Izmit, NNAF) is closed to the sensitivity threshold of the lake for the Core IZN19_31, while it is below the detection limit for the Core IZN19_21. On the top of the Core IZN19_31, only one turbidite layer is observed, which could correspond to this earthquake (*Fig. 8*a). The other two earthquakes near the sensitivity threshold (1719 and 1894 CE) actually probably not exceed the sensitivity threshold due to the significant uncertainties on the historical data (precise location and magnitude) (*Fig. 8*c). The strong correlation between historical and instrumental recordings and our sedimentary records supported the reliability of this conceptual approach. These results prove that Lake Iznik's sediments record the past regional seismicity on the different branches of the NAF system. Upcoming studies should take into account sediment cores from different sub-basins of Lake Iznik. It will help to distinguish more accurately the source(s) of such coarser grained deposits, their synchronicity in different independent locations being a strong argument for their seismic trigger (e.g. Van Daele et al., 2015).

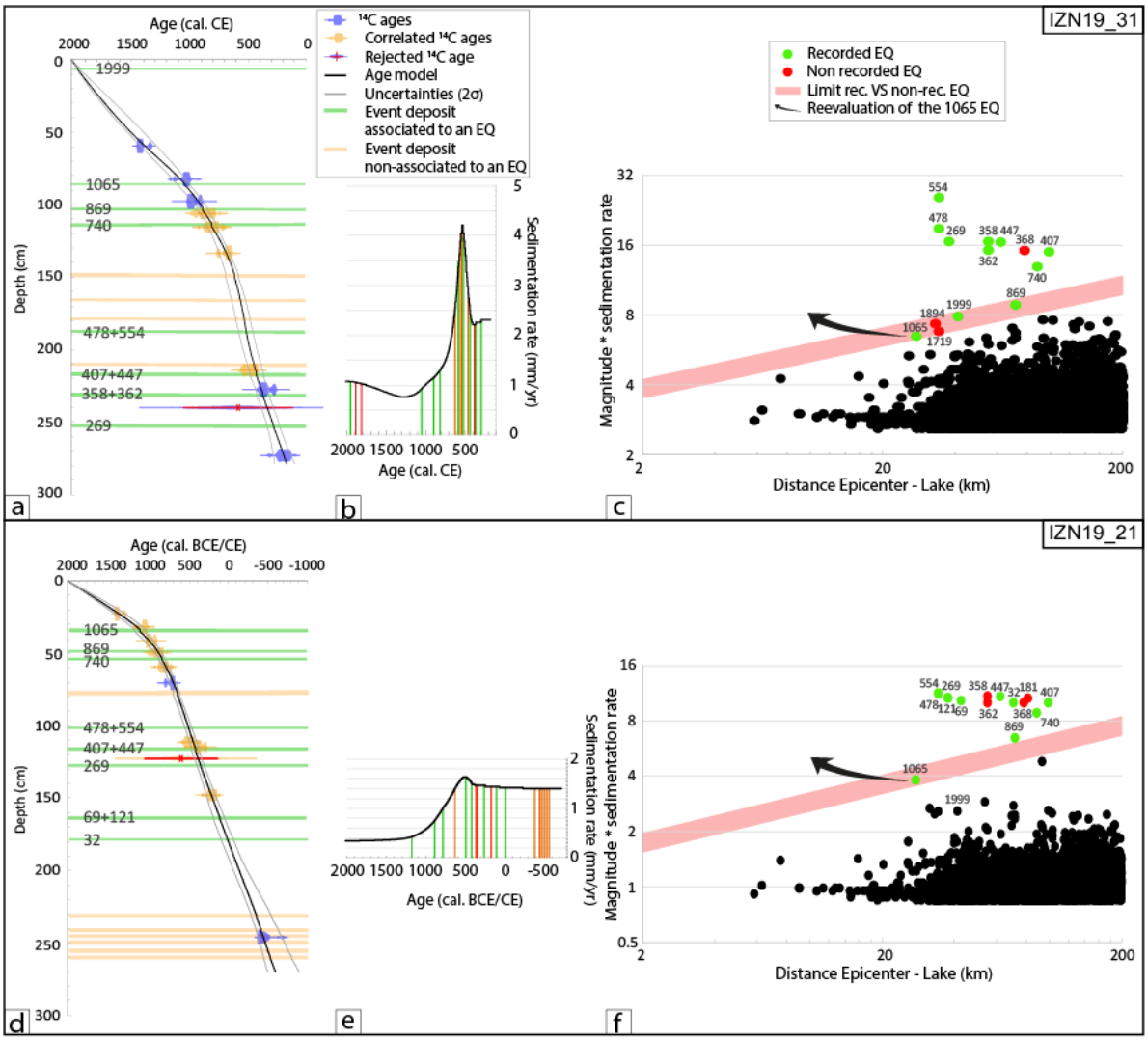

Fig. 8: Diagrams displaying for cores IZN19_31 and IZN19_21 (a, d) the interpreted age models. (b, e) The sedimentation rate variations through time. The green lines represent the event deposits associated to an earthquake as opposed to the orange lines. Red lines represent times at which earthquakes happened without event deposit in the sediment cores. (c, f) Conceptual plots presenting the distance of earthquake epicenters to Lake Iznik (40.406N, 29.673E as reference) versus earthquake magnitudes multiply by the sedimentation rate averaged over the previous 100 years. The red thick line delimits the best fit versus recorded and non-recorded earthquakes. Black dots represent earthquakes below the best fit line which are not recorded in the lake. The black arrows show where the 1065 CE earthquake should be located in the diagram as the Iznik fault ruptured in the lake at that time (see below in the text).

5.2 Discovery of two hitherto unknown subaquatic faults

The bathymetric survey carried out in the lake allows to identify two previously unknown underwater faults (*Fig. 2* and *Fig. 3*). The first one is located in the northern sub-basin; striking SW-NE, this fault lineament shows a sharp vertical scarp of ~5 m (*Fig. 3*c), it forming the northward edge of the northern sub-basin and the shoreward underwater terraces (*Fig. 2*a and *Fig. 3*c). This fault segment is parallel and very close to the Boyalıca fault. We consider it is a segment of the Boyalıca fault. The terraces, with depths of 20, 40, and 45 m b.l.l. are interpreted as markers of past low lake levels as documented in the Gemlik Bay (Eriş et al., 2019). Based on the lake's shorelines, resembling the shape of a peanut and on general analysis of the entire bathymetric data set (Fig. 2), a left-lateral fault with a small normal component is inferred for the Boyalıca Fault. Microseismic data also document an oblique and normal movement on this fault during a Ms 2 earthquake (Gurbuz et al., 2000). Similar SW-NE sinistral faults are observed at the NAF scale, in the Gemlik Bay (Fig. 1) or associated to the NNAF where they comprise antithetic shear components (Alpar & Yaltırak, 2002; Kurtuluş & Canbay, 2007).

The second fault discovered in Lake Iznik - termed Iznik Fault - strikes E-W and separates the southern sub-basin from the central ridge (*Fig. 2*). The high-resolution seismic profile across IFS2 shows a series of steep faults interpreted to be arranged en-echelon manner (*Fig. 4, Profile P3*) suggesting that it presents mostly a strike-slip movement. The Iznik Fault seams to cross the entire lake; its eastern prolongation joins the dextral Dırazali Fault onshore and potentially the dextral Gemlik Fault to the west (*Fig. 3*), which would suggest a right-lateral component for this fault.

These two subaquatic faults are most likely still active as expressed by the morphological step observed on the lake floor. In particular for the Iznik Fault as indicates by the change in sedimentation rate across the structure and the occurrence of many pock marks indicating fluid escape along the fault, which are favored by deep-seated pathways along the buried fault plane (*Fig. 3b*).

5.3 Identification of the last earthquake rupture on the Iznik Fault

The core-to-core correlation across the Iznik Fault (IFS1 on *Fig. 3*a) allows to identify thicknesses variations of sedimentary units across the structure. For the present-day profile (*Fig.* 9a), the topography is deduced from the multibeam bathymetry (Profile P1 on *Fig.* 3a). From the sediment-core analysis we retrieved the paleotopography and sedimentological features at different moments by removing layer by

layer from the top to the bottom of the cores. For each depth, the age is determined from the age models of cores IZN19_21 and IZN19_31 (*Fig.* 7); the total uncertainty range of the different ages allows to encompass the time span. After removing the pink and green units (*Fig.* 9b), the residual topography is assumed to be the paleo topography at 1010/1182 cal CE. Compaction and erosion are neglected on this reconstruction, as we suppose a similar effect on both sides of the fault as well as similar erosional processes (e.g. deep currents). This reconstruction highlights a sediment thickness variation of ~50 cm between the hanging and the footwall of the fault for the green layer (*Fig.* 9). These thickness variation reflect the fault activity. The co-seismic and vertical offset created an accommodation space on the footwall which then has been gradually filled (*Fig.* 9b). The observation of an event deposit at the base of this green unit also supports this interpretation of fault rupture (*Fig. 8*a). The turbidity current-induced deposit is a co-seismic marker while the sedimentary thickness variation is a syn- to post-seismic indicator; as it has also been observed in the Sea of Marmara along the NNAF (Armijo et al., 2005). This co-seismic event deposit is dated between 1010 to 1182 cal. CE that coincides with the well-documented 1065 CE earthquake (Ambraseys, 2009). The independent archeo-seismological study of Benjelloun, (2017) documents an important phase the destruction-reconstruction for the buildings in Nicaea (formerly Iznik) between 858 and 1097 CE. According to the original historical archive (Michael & Attaleiatēs, 2012), the 1065 CE earthquake has strongly damaged the city of Iznik (formerly Nicaea/ Nikaia): “It happened at Nikaia in Bithynia and brought almost total devastation and ruin to the place. Its most important and large churches [...] and the one of the Holy Fathers, where the Council of the most Holy and Orthodox Fathers against Areios confirmed its decisions [...] those churches, then, were shaken and collapsed as did the walls of the city along with many private dwellings.”. No other locality seems to have been damaged as strongly as Iznik during this earthquake, which suggests a proximal event rupturing the MNAF. The ~50 cm vertical co-seismic offset could have also triggered a destructive wave (tsunami) or a lake-level variation that led to the destruction and submersion of the basilica of Nicaea (Şahin, 2014), explaining why this basilica has never been rebuilt. The most recent layer (pink in *Fig. 9*a) dated to post 1521/1734 cal. CE shows a thickness increase of ~44 cm in the southernmost shore-proximal Core IZN19_04. Bathymetric data suggest a recent delta-derived clastic contribution to explain this thickness variation. The recent increase of erosion and sediment supply to the lake is likely related to agriculture revival in the catchment (Geyer et al., 2001). The lowermost stratigraphic unit found in our cores, the unit marked in grey, is 62 cm thicker on

the southern side of the fault (62 cm vs. <130 cm) (*Fig. 9*c). Such a variation could be also caused by vertical movements of the fault during former earthquakes before the common era, but longer sequences are required to retrieved the base of the grey layer and infer the pre-grey layer topography prior the grey layer to confirm this hypothesis. Further seismic acquisitions could also help to highlight and image stratigraphically deeper units in the hanging wall (e.g. Beck et al., 2012).

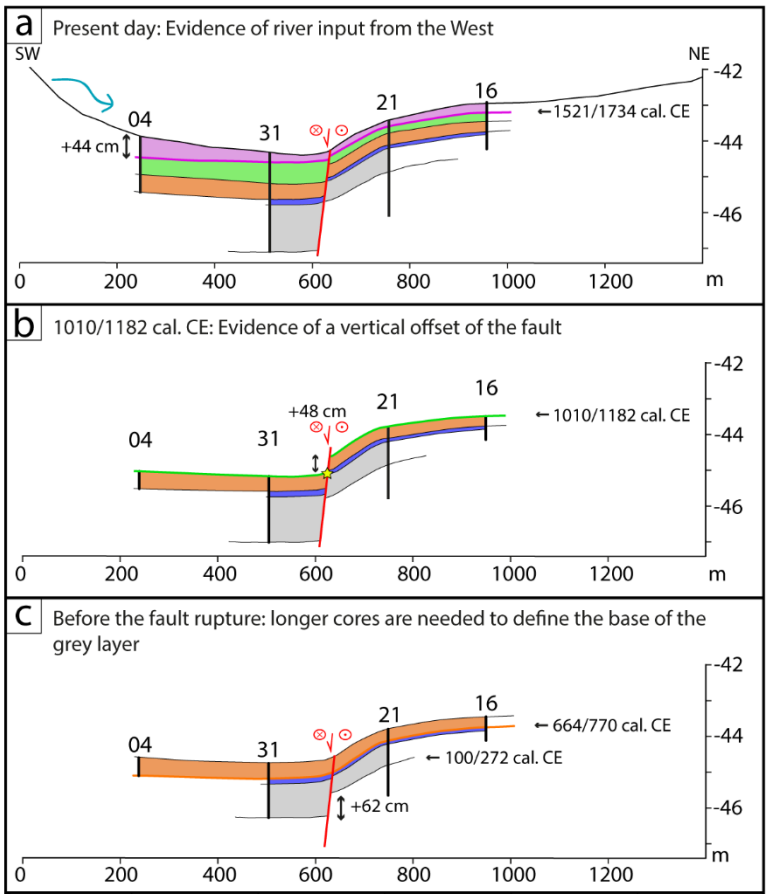

Core / Period	04	31	21	16	03
> 1521/1734 cal. CE	+44	+4	16	+8	+4
> 1010/1182 cal. CE	+32	+48	18	+4	+12
> 664/770 cal. CE	+12	+10	36	-8	-2
> 598/705 cal. CE	?	3	9	-4	-3
> 100/272 cal. CE	?	+62	73	?	?

Fig. 9: Conceptual diagrams presenting the (paleo)topography and sedimentological reconstructions at three different times. The location of the cores, the distance between each core, their length and the thickness of the different units are drawn to scale. (a) Present day: evidence of river input from the West.

566 *The topography is obtained from our bathymetric data (b) at 1010/1182 cal. CE*: e*vidence of a ~50 cm*
567 *vertical offset on the fault (c) before the last fault rupture. The table represents the deviation in sediment*
568 *thicknesses (in cm) for each core and stratigraphic unit relative to Core IZN19_21. The colors are the*
569 *same as in Fig. 6.*

570 ### 5.4 Regional implications

571 Linear strike-slip faults such as the Iznik Fault are important tectonic structures as shown by the one
572 discovered within the Lake Sapanca during the Izmit 1999 earthquake, along the NNAF (Polonia et al.,
573 2004). The rupture along this straight segment was of supershear nature and caused strong damages
574 amplified by ground liquefaction (Bouchon, 2002). The presented newly discovered faults provide essential
575 data to better assess the seismic hazard of the region.
576 The description of the whole active fault system in and around Lake Iznik also improves tectonic
577 knowledge. Lake Iznik exhibits three sub-basins that cannot be explained in a simple pull-apart process
578 approach (Wu et al., 2009; Dooley & Schreurs, 2012). The left-lateral Boyalıca Fault presented in this
579 study delimits the western sub-basin from the two others (*Fig. 10*a, b). The Gürle and Orhangazi normal
580 faults bounded the underwater Iznik and Boyalıca strike-slip faults, resulting in a negative flower structure
581 as shown on the simplified NS cross section of the lake (*Fig. 10*c*)*. The basin can thus be divided into three
582 blocks separated by both the left- and right-lateral strike-slip faults document in this study (*Fig. 10*b).
583 Overall, these rather E-W faults show minor vertical displacements suggesting they are mostly strike-slip
584 faults. Similar geometry with basins limited by such faults are observed on models of transtensional pull-
585 apart basins, due to an oblique and divergent displacement at a θ angle with the main strike-slip fault (Wu
586 et al., 2009; Dooley & Schreurs, 2012; *Fig. 10*a). The discovery of the Iznik strike-slip Fault also suggests
587 fault partitioning of the MNAF close to Lake Iznik. The onshore Gürle Fault accommodates mostly the
588 normal component whereas the Iznik Fault seems accommodates most of the right-lateral component of the
589 MNAF system, controlling the shape of the southern sub-basin (*Fig. 10*). In addition to the faults
590 mentioned above that control the sub-basins, other segments lead to the complex configuration of the Iznik
591 Basin. Two extensional structures have been previously studied on the western sub-basin (Öztürk et al.,
592 2009) and to the East of the city of Iznik (the Ebeyli Fault) (Benjelloun et al., 2018). The bathymetric data
593 from the DSI highlights different other scarps that need to be studied more closely (*Fig. 10*a). The
594 combination of all these new observations clarifies that (1) the isolated circular western sub-basin seems to

be less deformed and may correspond to a former pull apart, as suggested by its form (2) the formation of the two other elongated sub-basins may be caused by a transtensional motion and (3) the highest central ridge limited by both Boyalıca and Iznik faults is also link to the transtensional movement (Fig. 10b). Given the geological inheritance of this region (e.g. Şengör & Yilmaz, 1981), it is probable that certain fault segments and in particular that of Boyalica, had different components over tectonic phases due to stress field variations during the evolution of the basin, and undergone possible rotations and/or deactivation/reactivation. Further bathymetric and seismic surveys will provide key elements to understand the timing of these tectonic controls.

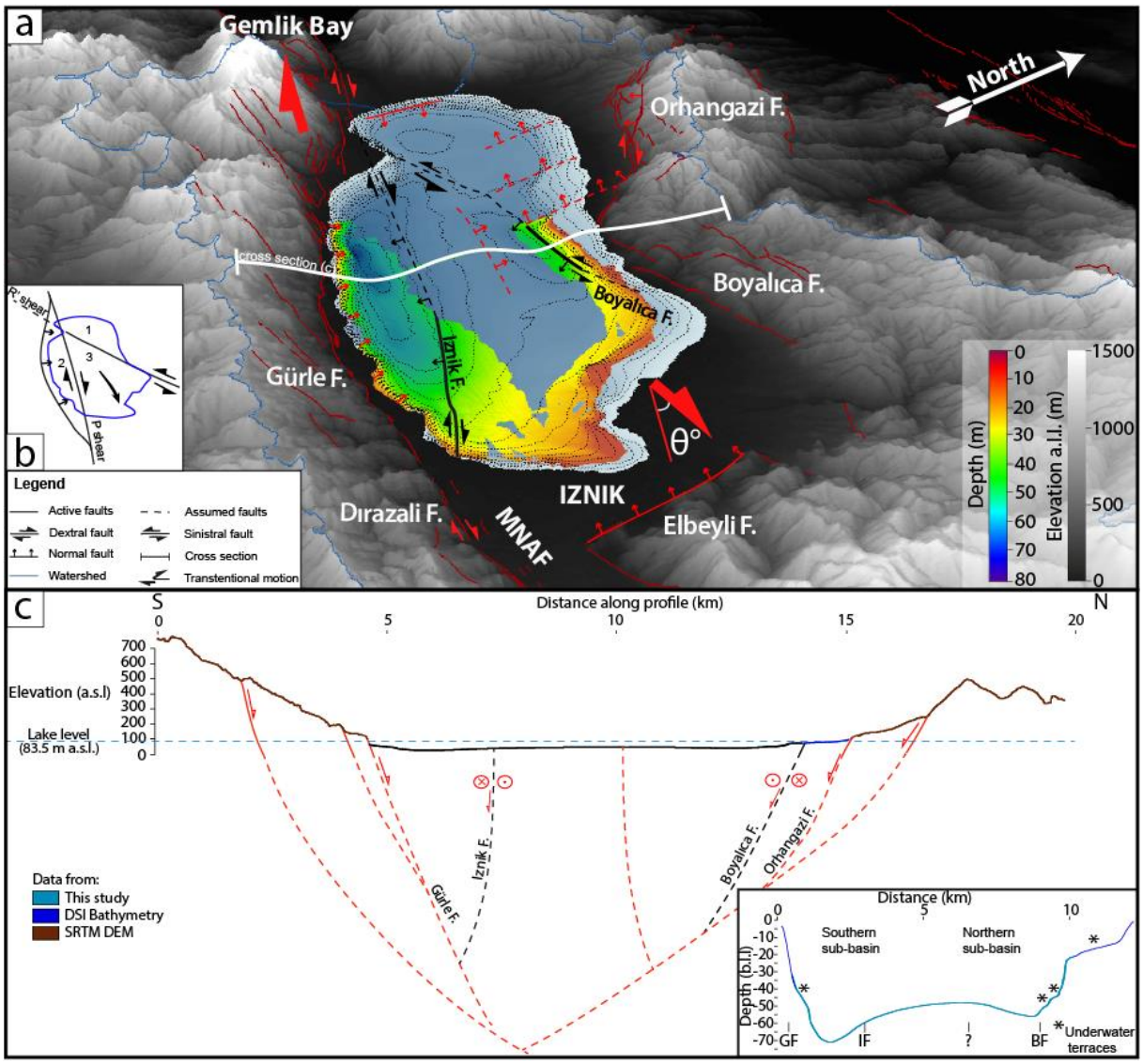

Fig. 10: (a) 3D visualization derived from SRTM DEM (1 arc-second resolution) of the Iznik Basin with tectonic interpretation. The bathymetry carried out in this study is superimposed on the DSI bathymetry. The red solid lines are active faults from the literature (Benjelloun, 2017; Emre et al., 2018), whereas the

red dashed lines represent presumed faults. The black lines represent newly discovered fault structures documented in this study. The blue line represents the limit of the catchment of Lake Iznik. (b) Simplified tectonic context of the Iznik Basin. (c) N-S profile across the lake (see (a) for location), with tectonic interpretation. The black fault lines represent the two faults documented in this study. Inset is a zoom of the lake bathymetry. GF: Gürle Fault; IF: Iznik Fault; BF: Boyalıca Fault.

6. Conclusions

The sedimentary study done on the cores sampled in the Lake Iznik revealed fourteen earthquake-induced turbidite deposits since their ages correspond to historical regional seismic events during the past two millennia, allowing to refine the calendar of historical seismicity in this region.

The combined geophysical and sedimentological approach in Lake Iznik allows to discover two active subaquatic faults: a segment of the Boyalıca Fault and the Iznik Fault that form part of the middle strand of the North Anatolian Fault and that are responsible for some of the recorded earthquakes in the lake. The sedimentological study focused on both part of the Iznik Fault shows paleo-seismological evidences for a last rupture that occurred during the devastating 1065 CE earthquake. Studying longer sequences from the same locations associated to on-fault studies could provide new insights about the earthquake recurrence interval on this specific fault which seems to be longer than 1000 years. The seismic gap since 1065 of this Iznik Fault segment strongly increases the seismic hazard in the region of Iznik and must be taken into account for the seismic risk assessment of the NAF system.

Finally, our findings provide a better understanding of the Lake Iznik tectonic context that present negative flower structure due to and important transtensional movement.

Acknowledgments

This investigation was conducted in the framework of “BASILIZNIK-SECRETS” project funded by the French ANR CE03-2019 BASILIZNIK-SECRETS, the IRS-IDEX UGA project “BASILIZNIK”, and the INSU ALEAS program (France) Basiliznik. The Kingdom Suite license was provided by IHS Markit through a University Grant Program. The authors would like to thank the Turkish Ministry of Culture and Tourism for permitting core sampling and geophysical surveying in Lake Iznik; the archeological research team of Prof. M. Şahin and all the students (K. Kayacan, S. Cura, M. Çınar) from the archaeological laboratory of the Uludağ University of Bursa for their precious support in the field. We are also grateful to

the excellent services of Captain C. Çelikbilek who maneuvered us on his Vessel safely across the lake. The authors would like to thank EDYTEM laboratory for the X-ray fluorescence analyses and F. Soufi for his involvement in the realization of the thin sections. We also thank N. Findling for his precious help during the SEM observation sessions at ISTerre laboratory and I. Akalan Gündüz for our discussions dealing with the historical data and her help on the field.

Data availability

Supplementary data reported in this study are given in the supporting informations and all core and geophysical data are stored in Pangaea database at: **pending**.

Author contributions

RG performed the analysis and wrote the main manuscript file and figures. JS designed the research project. PS dynamically assisted throughout the whole research process, during all stages of analysis and interpretations of the cores. SF and FA led the bathymetric campaign and assisted the geophysical data processing. RG, JS, SF, FA, SG sampled the cores. ALD assisted acquisition and interpretation of XRF analysis. MŞ and SG provided invaluable assistance during the different field campaigns. CG and FN provided the seismic data from a previous field campaign. JS, PS, SF, FA and CG actively corrected and improved the manuscript. Each author has proofread and corrected the manuscript at least once.

References

Alpar, B., & Yaltırak, C. (2002). Characteristic features of the North Anatolian Fault in the eastern Marmara region and its tectonic evolution. *Marine Geology*, *190*(1–2), 329–350.

Ambraseys. (2002). The Seismic Activity of the Marmara Sea Region over the Last 2000 Years. *Bulletin of the Seismological Society of America*, *92*(1), 1–18. https://doi.org/10.1785/0120000843

Ambraseys. (2009). *Earthquakes in the Mediterranean and Middle East: a multidisciplinary study of seismicity up to 1900*. Cambridge University Press.

Ambraseys, & Finkel, C. (1991). Long-term seismicity of Istanbul and of the Marmara Sea region. *Terra Nova*, *3*(5), 527–539.

Ambraseys, N. N., & Jackson, J. A. (2000). Seismicity of the Sea of Marmara (Turkey) since 1500. *Geophysical Journal International*, *141*(3), F1–F6. https://doi.org/10.1046/j.1365-246x.2000.00137.x

663 Armijo, R., Pondard, N., Meyer, B., Uçarkus, G., de Lépinay, B. M., Malavieille, J., et al. (2005).
664 Submarine fault scarps in the Sea of Marmara pull-apart (North Anatolian Fault): Implications for
665 seismic hazard in Istanbul. *Geochemistry, Geophysics, Geosystems*, *6*(6).
666 Arnaud, F., Poulenard, J., Giguet-Covex, C., Wilhelm, B., Révillon, S., Jenny, J.-P., et al. (2016). Erosion
667 under climate and human pressures: An alpine lake sediment perspective. *Quaternary Science*
668 *Reviews*, *152*, 1–18. https://doi.org/10.1016/j.quascirev.2016.09.018
669 Avşar, U., Hubert-Ferrari, A., De Batist, M., Schmidt, S., & Fagel, N. (2015). Sedimentary records of past
670 earthquakes in Boraboy Lake during the last ca 600 years (North Anatolian Fault, Turkey).
671 *Palaeogeography, Palaeoclimatology, Palaeoecology*, *433*, 1–9.
672 https://doi.org/10.1016/j.palaeo.2015.04.031
673 Bajard, M., Poulenard, J., Sabatier, P., Develle, A.-L., Giguet-Covex, C., Jacob, J., et al. (2017).
674 Progressive and regressive soil evolution phases in the Anthropocene. *CATENA*, *150*, 39–52.
675 https://doi.org/10.1016/j.catena.2016.11.001
676 Barka, A. (1993). Kuzey Anadolu Fayının Sapanca-İzmit ve Geyve-İznik kolları üzerinde paleosismik
677 araştırmalar. *TÜBİTAK Proje No: YBAG-4/7551*, 85.
678 Beck, C., Reyss, J.-L., Leclerc, F., Moreno, E., Feuillet, N., Barrier, L., et al. (2012). Identification of deep
679 subaqueous co-seismic scarps through specific coeval sedimentation in Lesser Antilles: implication
680 for seismic hazard. *Natural Hazards and Earth System Sciences*, *12*(5), 1755–1767.
681 https://doi.org/10.5194/nhess-12-1755-2012
682 Beck, Christian. (2009). Late Quaternary lacustrine paleo-seismic archives in north-western Alps:
683 Examples of earthquake-origin assessment of sedimentary disturbances. *Earth-Science Reviews*,
684 *96*(4), 327–344.
685 Benjelloun, Y. (2017). *The middle strand of the North Anatolian fault in Iznik region : insights from*
686 *geomorphology and archeoseismology* (Doctoral dissertation). Université Grenoble Alpes.
687 Retrieved from https://tel.archives-ouvertes.fr/tel-01952234
688 Benjelloun, Yacine, de Sigoyer, J., Dessales, H., Garambois, S., & Şahin, M. (2018). Construction history
689 of the aqueduct of Nicaea (Iznik, NW Turkey) and its on-fault deformation viewed from
690 archaeological and geophysical investigations. *Journal of Archaeological Science: Reports*, *21*,
691 389–400. https://doi.org/10.1016/j.jasrep.2018.08.010

692 Blaauw, M. (2010). Methods and code for 'classical'age-modelling of radiocarbon sequences. *Quaternary*
693 *Geochronology*, *5*(5), 512–518.
694 Bouchon, M. (2002). Space and Time Evolution of Rupture and Faulting during the 1999 Izmit (Turkey)
695 Earthquake. *Bulletin of the Seismological Society of America*, *92*(1), 256–266.
696 https://doi.org/10.1785/0120000845
697 Brocard, G., Anselmetti, F. S., & Teyssier, C. (2016). Guatemala paleoseismicity: from Late Classic Maya
698 collapse to recent fault creep. *Scientific Reports*, *6*, 36976.
699 Cetin, K. O., Youd, T. L., Seed, R. B., Bray, J. D., Sancio, R., Lettis, W., et al. (2002). Liquefaction-
700 induced ground deformations at Hotel Sapanca during Kocaeli (Izmit),Turkey earthquake. *Soil*
701 *Dynamics and Earthquake Engineering*, *22*(9–12), 1083–1092. https://doi.org/10.1016/S0267-
702 7261(02)00134-3
703 Doğan, B. (2010). *Kuzey Anadolu Fay Sistemi Güney Kolunun Geyve-gemlik Arasındaki Kesiminin*
704 *Morfotektonik, Tektonostratigrafik Ve Paleosismolojik Evrimi* (PhD Thesis). Fen Bilimleri
705 Enstitüsü.
706 Doğan, B., Tüysüz, O., & Şanlı, F. B. (2015). Tectonostratigraphic evolution of the basins on the southern
707 branch of the North Anatolian Fault System in the SE Marmara Region, Turkey. *International*
708 *Journal of Earth Sciences*, *104*(2), 389–418. https://doi.org/10.1007/s00531-014-1083-9
709 Dooley, T. P., & Schreurs, G. (2012). Analogue modelling of intraplate strike-slip tectonics: A review and
710 new experimental results. *Tectonophysics*, *574*, 1–71.
711 EarthExplorer - Home. (n.d.). Retrieved June 15, 2020, from https://earthexplorer.usgs.gov/
712 Emre, Ö., Duman, T. Y., Özalp, S., Şaroğlu, F., Olgun, Ş., Elmacı, H., & Çan, T. (2018). Active fault
713 database of Turkey. *Bulletin of Earthquake Engineering*, *16*(8), 3229–3275.
714 https://doi.org/10.1007/s10518-016-0041-2
715 Ergintav, S., Reilinger, R., Çakmak, R., Floyd, M., Cakir, Z., Doğan, U., et al. (2014). Istanbul's
716 earthquake hot spots: Geodetic constraints on strain accumulation along faults in the Marmara
717 seismic gap. *Geophysical Research Letters*, *41*(16), 5783–5788.
718 Eriş, K. K., Sabuncu, A., Gasperini, L., Polonia, A., & Kındap, T. (2019). Influence of climate on the late
719 Pleistocene depositional history of the Gulf of Gemlik (Sea of Marmara). *Geo-Marine Letters*,
720 *39*(3), 205–221.

721 Evans, J. A. S. (2005). *The Emperor Justinian and the Byzantine Empire*. Greenwood Publishing Group.

722 Geyer, martin, & al. (2001). *Castrum 7: Zones côtières littorales dans le monde Méditerranéen au Moyen*
723 *Âge : défense, peuplement, mise en valeur*. Casa de Velázquez.

724 Girardclos, S., Schmidt, O. T., Sturm, M., Ariztegui, D., Pugin, A., & Anselmetti, F. S. (2007). The 1996
725 AD delta collapse and large turbidite in Lake Brienz. *Marine Geology*, *241*(1–4), 137–154.

726 Guevara, S. R., Rizzo, A., Daga, R., Williams, N., & Villa, S. (2019). Bromine as indicator of source of
727 lacustrine sedimentary organic matter in paleolimnological studies. *Quaternary Research*, *92*(1),
728 257–271.

729 Guidoboni, E., Comastri, A., Traina, G., & Geofisica, R. I. N. di. (1994). *Catalogue of Ancient Earthquakes*
730 *in the Mediterranean Area up to the 10th Century*. Istituto nazionale di geofisica Rome.

731 Guidoboni, E., Comastri, A., Storia, S., & others. (2005). *Catalogue of Earthquakes and Tsunamis in the*
732 *Mediterranean Area from the 11th to the 15th Century*.

733 Gurbuz, C., Aktar, M., Eyidogan, H., Cisternas, A., Haessler, H., Barka, A., et al. (2000). The
734 seismotectonics of the Marmara region (Turkey): results from a microseismic experiment.
735 *Tectonophysics*, *316*(1), 1–17. https://doi.org/10.1016/S0040-1951(99)00253-X

736 Hage, S., Hubert-Ferrari, A., Lamair, L., Avşar, U., El Ouahabi, M., Van Daele, M., et al. (2017). Flow
737 dynamics at the origin of thin clayey sand lacustrine turbidites: Examples from Lake Hazar,
738 Turkey. *Sedimentology*, *64*(7), 1929–1956. https://doi.org/10.1111/sed.12380

739 Heiri, O., Lotter, A. F., & Lemcke, G. (2001). Loss on ignition as a method for estimating organic and
740 carbonate content in sediments: reproducibility and comparability of results. *Journal of*
741 *Paleolimnology*, *25*(1), 101–110.

742 Hilbe, M., & Anselmetti, F. S. (2014). Signatures of slope failures and river-delta collapses in a perialpine
743 lake (Lake Lucerne, Switzerland). *Sedimentology*, *61*(7), 1883–1907.
744 https://doi.org/10.1111/sed.12120

745 Honkura, Y., & Işikara, A. M. (1991). Multidisciplinary research on fault activity in the western part of the
746 North Anatolian Fault Zone. *Tectonophysics*, *193*(4), 347–357. https://doi.org/10.1016/0040-
747 1951(91)90343-Q

748 Hubert-Ferrari, A., Barka, A., Jacques, E., Nalbant, S. S., Meyer, B., Armijo, R., et al. (2000). Seismic
749 hazard in the Marmara Sea region following the 17 August 1999 Izmit earthquake. *Nature*,
750 *404*(6775), 269–273. https://doi.org/10.1038/35005054
751 Hubert-Ferrari, A., Lamair, L., Hage, S., Schmidt, S., Çağatay, M. N., & Avşar, U. (2020). A 3800 yr
752 paleoseismic record (Lake Hazar sediments, eastern Turkey): Implications for the East Anatolian
753 Fault seismic cycle. *Earth and Planetary Science Letters*, *538*, 116152.
754 Kurtuluş, C., & Canbay, M. M. (2007). Tracing the middle strand of the North Anatolian Fault Zone
755 through the southern Sea of Marmara based on seismic reflection studies. *Geo-Marine Letters*,
756 *27*(1), 27–40. https://doi.org/10.1007/s00367-006-0050-2
757 Le Pichon, X., İmren, C., Rangin, C., Şengör, A. M. C., & Siyako, M. (2014). The South Marmara Fault.
758 *International Journal of Earth Sciences*, *103*(1), 219–231. https://doi.org/10.1007/s00531-013-
759 0950-0
760 Michael, A., & Attaleiatēs, M. (2012). *The History* (Vol. 16). Harvard University Press.
761 Miebach, A., Niestrath, P., Roeser, P., & Litt, T. (2016). Impacts of climate and humans on the vegetation
762 in northwestern Turkey: palynological insights from Lake Iznik since the Last Glacial. *Climate of*
763 *the Past*, *12*(2), 575–593. https://doi.org/10.5194/cp-12-575-2016
764 Moernaut, J., Van Daele, M., Strasser, M., Clare, M. A., Heirman, K., Viel, M., et al. (2017). Lacustrine
765 turbidites produced by surficial slope sediment remobilization: A mechanism for continuous and
766 sensitive turbidite paleoseismic records. *Marine Geology*, *384*, 159–176.
767 https://doi.org/10.1016/j.margeo.2015.10.009
768 Monecke, K., Anselmetti, F. S., Becker, A., Sturm, M., & Giardini, D. (2004). The record of historic
769 earthquakes in lake sediments of Central Switzerland. *Tectonophysics*, *394*(1–2), 21–40.
770 Munsell Color. (1994). *Munsell Soil Color Charts. Macbeth, Division of Kollmorgen Instruments*
771 *Corporation*. Newburgh, NY: Munsell Color.
772 Öcal, A. (2019). Natural Disasters in Turkey: Social and Economic Perspective. *International Journal of*
773 *Disaster Risk Management*, *1*(1), 51–61.
774 Özalp, S., Emre, Ö., & Dogan, A. (2013). The segment structure of southern branch of the North Anatolian
775 Fault and paleoseismological behaviour of the Gemlik Fault, NW Anatolia. *General Directorate of*
776 *Mineral Research and Exploration (MTA) Bulletin*, *147*, *1–17*.

Öztürk, K., Yaltirak, C., & Alpar, B. (2009). The relationship between the tectonic setting of the Lake Iznik basin and the middle strand of the North Anatolian Fault. *Turkish Journal of Earth Sciences*, *18*(2), 209–224.

Parsons, T. (2000). Heightened Odds of Large Earthquakes Near Istanbul: An Interaction-Based Probability Calculation. *Science*, *288*(5466), 661–665. https://doi.org/10.1126/science.288.5466.661

Polonia, A., Gasperini, L., Amorosi, A., Bonatti, E., Bortoluzzi, G., Cagatay, N., et al. (2004). Holocene slip rate of the North Anatolian Fault beneath the Sea of Marmara. *Earth and Planetary Science Letters*, *227*(3–4), 411–426.

R Core Team. (2018). *R: A Language and Environment for Statistical Computing*. Vienna, Austria: R Foundation for Statistical Computing. Retrieved from https://www.R-project.org/

Rapuc, W., Sabatier, P., Andrič, M., Crouzet, C., Arnaud, F., Chapron, E., et al. (2018). 6600 years of earthquake record in the Julian Alps (Lake Bohinj, Slovenia). *Sedimentology*, *65*(5), 1777–1799. https://doi.org/10.1111/sed.12446

Reilinger, R., McClusky, S., Vernant, P., Lawrence, S., Ergintav, S., Cakmak, R., et al. (2006). GPS constraints on continental deformation in the Africa-Arabia-Eurasia continental collision zone and implications for the dynamics of plate interactions. *Journal of Geophysical Research: Solid Earth*, *111*(B5).

Reimer, P. J., Bard, E., Bayliss, A., Beck, J. W., Blackwell, P. G., Ramsey, C. B., et al. (2013). IntCal13 and Marine13 radiocarbon age calibration curves 0–50,000 years cal BP. *Radiocarbon*, *55*(4), 1869–1887.

Richter, T. O., Van der Gaast, S., Koster, B., Vaars, A., Gieles, R., de Stigter, H. C., et al. (2006). The Avaatech XRF Core Scanner: technical description and applications to NE Atlantic sediments. *Geological Society, London, Special Publications*, *267*(1), 39–50.

Roeser, P., Franz, S. O., & Litt, T. (2016). Aragonite and calcite preservation in sediments from Lake Iznik related to bottom lake oxygenation and water column depth. *Sedimentology*, *63*(7), 2253–2277. https://doi.org/10.1111/sed.12306

Roeser, P. A., Franz, S. O., Litt, T., Ülgen, U. B., Hilgers, A., Wulf, S., et al. (2012). Lithostratigraphic and geochronological framework for the paleoenvironmental reconstruction of the last ~36 ka cal BP

805 from a sediment record from Lake Iznik (NW Turkey). *Quaternary International*, *274*, 73–87.
806 https://doi.org/10.1016/j.quaint.2012.06.006
807 Roodenberg, J. (2013). Change in food production and its impact on an early 6th millennium community in
808 northwest Anatolia. The example of Ilıpınar. *Praehistorische Zeitschrift*, *87*(2), 223–235.
809 Sabatier, P., Dezileau, L., Briqueu, L., Colin, C., & Siani, G. (2010). Clay minerals and geochemistry
810 record from northwest Mediterranean coastal lagoon sequence: Implications for paleostorm
811 reconstruction. *Sedimentary Geology*, *228*(3–4), 205–217.
812 Şahin, M. (2014). İznik Gölü'ndeki Batık Kilise: Deprem Kurbanı Aziz Neophytos. *Aktüel Arkeoloji 38*,
813 *Nisan, 8-10*.
814 Şahin, M., & R. Fairchild, M. (2018). Nicea's Underwater Basilica. *Biblical Archaeology, Review 44:6.*
815 Schnellmann, M., Anselmetti, F. S., Giardini, D., & McKENZIE, J. A. (2005). Mass movement-induced
816 fold-and-thrust belt structures in unconsolidated sediments in Lake Lucerne (Switzerland).
817 *Sedimentology*, *52*(2), 271–289.
818 Şengör, A., Grall, C., İmren, C., Le Pichon, X., Görür, N., Henry, P., et al. (2014). The geometry of the
819 North Anatolian transform fault in the Sea of Marmara and its temporal evolution: implications for
820 the development of intracontinental transform faults. *Canadian Journal of Earth Sciences*, *51*(3),
821 222–242.
822 Şengör, A. C., & Yilmaz, Y. (1981). Tethyan evolution of Turkey: a plate tectonic approach.
823 *Tectonophysics*, *75*(3–4), 181–241.
824 Stein, R. S., Barka, A. A., & Dieterich, J. H. (1997). Progressive failure on the North Anatolian fault since
825 1939 by earthquake stress triggering. *Geophysical Journal International*, *128*(3), 594–604.
826 https://doi.org/10.1111/j.1365-246X.1997.tb05321.x
827 Strasser, M., Anselmetti, F. S., Fäh, D., Giardini, D., & Schnellmann, M. (2006). Magnitudes and source
828 areas of large prehistoric northern Alpine earthquakes revealed by slope failures in lakes. *Geology*,
829 *34*(12), 1005. https://doi.org/10.1130/G22784A.1
830 Strasser, M., Monecke, K., Schnellmann, M., & Anselmetti, F. S. (2013). Lake sediments as natural
831 seismographs: A compiled record of Late Quaternary earthquakes in Central Switzerland and its
832 implication for Alpine deformation. *Sedimentology*, *60*(1), 319–341.
833 https://doi.org/10.1111/sed.12003

Tibi, R., Bock, G., Xia, Y., Baumbach, M., Grosser, H., Milkereit, C., et al. (2001). Rupture processes of the 1999 August 17 Izmit and November 12 Düzce (Turkey) earthquakes. *Geophysical Journal International*, *144*(2), F1–F7.

Uçarkuş, G. (2002). *Gemlik Fay Zonu'nun Aktif Tektoniği* (Doctoral dissertation). İstanbul Teknik Üniversitesi.

Ülgen, U. B., Franz, S. O., Biltekin, D., Çagatay, M. N., Roeser, P. A., Doner, L., & Thein, J. (2012). Climatic and environmental evolution of Lake Iznik (NW Turkey) over the last ~4700 years. *Quaternary International*, *274*, 88–101. https://doi.org/10.1016/j.quaint.2012.06.016

Van Daele, M., Moernaut, J., Doom, L., Boes, E., Fontijn, K., Heirman, K., et al. (2015). A comparison of the sedimentary records of the 1960 and 2010 great Chilean earthquakes in 17 lakes: Implications for quantitative lacustrine palaeoseismology. *Sedimentology*, *62*(5), 1466–1496. https://doi.org/10.1111/sed.12193

Viehberg, F. A., Ülgen, U. B., Damcı, E., Franz, S. O., Ön, S. A., Roeser, P. A., et al. (2012). Seasonal hydrochemical changes and spatial sedimentological variations in Lake Iznik (NW Turkey). *Quaternary International*, *274*, 102–111. https://doi.org/10.1016/j.quaint.2012.05.038

Wilhelm, B., Sabatier, P., & Arnaud, F. (2015). Is a regional flood signal reproducible from lake sediments? *Sedimentology*, *62*(4), 1103–1117. https://doi.org/10.1111/sed.12180

Wilhelm, B., Nomade, J., Crouzet, C., Litty, C., Sabatier, P., Belle, S., et al. (2016). Quantified sensitivity of small lake sediments to record historic earthquakes: Implications for paleoseismology: LAKE SENSITIVITY TO RECORD EARTHQUAKES. *Journal of Geophysical Research: Earth Surface*, *121*(1), 2–16. https://doi.org/10.1002/2015JF003644

Wu, J. E., McClay, K., Whitehouse, P., & Dooley, T. (2009). 4D analogue modelling of transtensional pull-apart basins. *Marine and Petroleum Geology*, *26*(8), 1608–1623. https://doi.org/10.1016/j.marpetgeo.2008.06.007

Yaltırak, C. (2002). Tectonic evolution of the Marmara Sea and its surroundings. *Marine Geology*, *190*(1–2), 493–529. https://doi.org/10.1016/S0025-3227(02)00360-2